Lawrence Berkeley National Laboratory

Recent Work

Title

Pion Correlations in Relativistic Heavy Ion Collisions for Three Symmetric Systems

Permalink

https://escholarship.org/uc/item/2b8558nr

Journal

Physical review C, 43(6)

Authors

Chacon, A.D.
Bistirlich, J.A.
Bossingham, R.R.
et al.
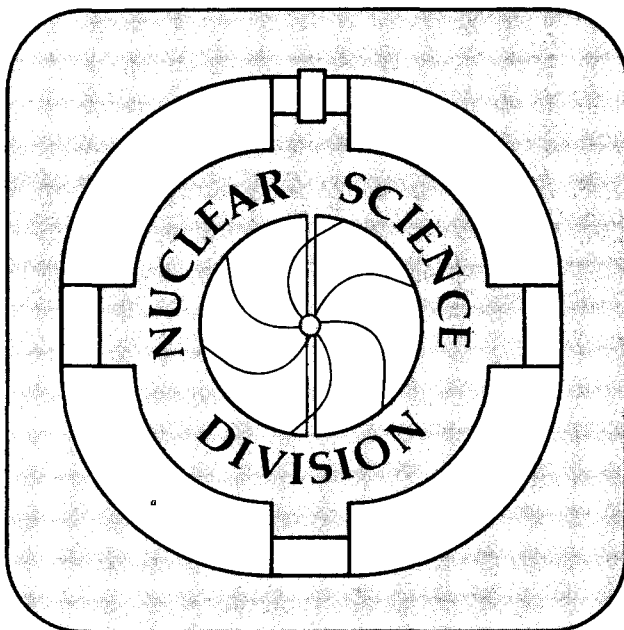
Publication Date

1991

Lawrence Berkeley Laboratory
UNIVERSITY OF CALIFORNIA

Pion Correlations in Relativistic Heavy Ion Collisions for Three Symmetric Systems

A.D. Chacon et al.

January 1991

NUCLEAR SCIENCE DIVISION

DISCLAIMER

Pion Correlations in Relativistic Heavy

Ion Collisions for Three Symmetric Systems

A. D. Chacon, J. A. Bistirlich, R. R. Bossingham,H. Bossy, H. R. Bowman,
C. W. Clawson,[*] K. M. Crowe, T. J. Humanic,[†] M. Justice, P. Kammel,[‡] J. M. Kurck,
S. Ljungfelt,[§] C. A. Meyer,[||] C. Petitjean,[¶] J. O. Rasmussen, M. A. Stoyer
Lawrence Berkeley Laboratory
University of California, Berkeley
Berkeley, California 94720

O. Hashimoto
Institute for Nuclear Study
University of Tokyo
Tanashi, Tokyo 188
Japan

Wm. C. McHarris
Michigan State University
East Lansing, Michigan 48824

J. P. Sullivan,[**] K. L. Wolf
Cyclotron Institute
Texas A & M University
College Station, Texas 77843

W. A. Zajc
Columbia University
New York, New York 10027

January 23, 1991

Abstract

The method of two-pion interferometry was used to obtain source-size and lifetime parameters for the pions produced in heavy ion collisions. Two acceptances (centered at approximately $0°$ and approximately $90°$, in the center of mass) were used for each of three systems, 1.70 GeV/nucleon ^{56}Fe + Fe, 1.82 GeV/nucleon ^{40}Ar + KCl and 1.54 GeV/nucleon ^{93}Nb + Nb, allowing a search for dependences on nuclear mass and viewing angle. The correlation functions were calculated by comparing data samples to event-mixed reference samples. The effect of the particle correlations on the reference samples was corrected by weighting the events appropriately to remove the residual correlation effect.

The source parameters, in the nucleus-nucleus center-of-mass frame show an oblate source (i.e., $R_\perp > R_\parallel$) for the lighter systems and an approximately spherical source for the heaviest system. The dependence on nuclear mass shows that $R_\perp$ is essentially constant (under both viewing angles), whereas $R_\parallel$ for the $90°$ (cm) data increases with the nuclear mass. No evidence was found for a dependence of the source size on the pion momentum.

PACS number 25.70.NP

Typeset Using REVTEX

I. INTRODUCTION

There are several motivations for measuring the pion source size in relativistic heavy ion collisions. The most obvious is that the measured source size can be compared to that predicted by one of the many nuclear collision simulation codes.[1] In principle, nuclear transport codes are capable of predicting source sizes, since all contain the geometry of the nuclear collision (see, for example, Padula et al.[2]). Another motivation is that, should nuclear collisions at higher energies produce long-lived forms of nuclear matter,[3,4] the source size and/or lifetime may not be a smooth function of the collision energy, and this can be revealed by measuring the source size as a function of the collision energy.

The measurement reported here was made using intensity interferometry, which is based on the interference of identical particles due to the Bose-Einstein symmetrization of the wave function. The interference induces a correlation of the emitted bosons as a function of their momentum difference known as the Goldhaber-Goldhaber-Lee-Pais (GGLP) effect,[5] and also as the Hanbury–Brown–Twiss (HBT) effect.[6] Negative pion interferometry was studied in the systems 1.82 GeV/nucleon ^{40}Ar + KCl, 1.70 GeV/nucleon ^{56}Fe + Fe and 1.54 GeV/nucleon ^{93}Nb + Nb, allowing a search for effects depending on the size of the nuclear system. The measurements were made for two different acceptances, centered at approximately 0°, and 45° in the laboratory (approximately 90° in the center of mass), permitting a search for effects depending on the viewing angle. The large data samples obtained in this experiment allowed source shape determinations, dropping the frequently made assumption that the pion source has a spherical shape. In the data samples for Fe + Fe, Nb + Nb, and for 0° Ar + KCl, the dependence on the pion momentum was studied. In addition, for

the Nb data, the dependence on the average momentum of the pions was studied to search for the theoretically predicted effects due to expansion of the pion source.[3,7,8] Some of the Fe results have been published in an earlier Letter[9] and are described here in more detail.

II. THEORY

A. Bose-Einstein Correlations

Suppose that the pions in a nuclear collision are emitted with momenta and energies $(\mathbf{p}, E)$ at positions and times $(\mathbf{r}, t)$ with a probability distribution for emission given by $\rho(\mathbf{r}, t)$. Then, assuming that the pions may be described by plane waves and that the pion sources act incoherently, the two-particle correlation function, the probability distribution for emission of two pions relative to the emission of the same particles without Bose-Einstein symmetrization, becomes[10]

$$C_2(\mathbf{p}_1, \mathbf{p}_2) = 1 + |\tilde{\rho}(\mathbf{q}, q_0)|^2 \, , \tag{1}$$

where

$$\mathbf{q} = \mathbf{p}_2 - \mathbf{p}_1 \tag{2}$$

$$q_0 = |E_2 - E_1| \tag{3}$$

$$\tilde{\rho}(\mathbf{q}, q_0) = \iint e^{i(\mathbf{q} \cdot \mathbf{x} - q_0 t)} \rho(\mathbf{x}, t) \, d^3\mathbf{x} \, dt \tag{4}$$

$$= \text{the Fourier transform of } \rho(\mathbf{x}, t).$$

Note that $|\tilde{\rho}(\mathbf{q}, q_0)|^2$ is an even function in both $\mathbf{q}$ and q_0, so that the absolute value in Eq. 3 is not necessary, and the order of $\mathbf{p}_1$ and $\mathbf{p}_2$ in Eq. 2 is arbitrary. In this work, natural units ($\hbar = c = 1$) are used.

4

B. The Correlation Function Used in this Analysis

The source density can be parameterized in several ways (see, for example, Zajc[11]). In this analysis, the source density $\rho(\mathbf{x}, t)$ is assumed to be a Gaussian in the center of mass of the colliding nuclei

$$\rho(\mathbf{x}, t) \propto \exp\left\{-\left(\frac{r_\perp}{R_\perp}\right)^2 - \left(\frac{r_\parallel}{R_\parallel}\right)^2 - \left(\frac{t}{\tau}\right)^2\right\} , \tag{5}$$

where the notations $\perp$ ($\parallel$) mean perpendicular (parallel) to the beam axis. The two radius parameters are $R_\perp$ and $R_\parallel$, while τ is the lifetime parameter. With this source density, the correlation function becomes

$$C_2(\mathbf{p}_1, \mathbf{p}_2) = 1 + \exp\left\{-\left(\frac{q_\perp^2 R_\perp^2}{2}\right) - \left(\frac{q_\parallel^2 R_\parallel^2}{2}\right) - \left(\frac{q_0^2 \tau^2}{2}\right)\right\} , \tag{6}$$

where $q_\perp$ ($q_\parallel$) is the component of $\mathbf{q}$ perpendicular (parallel) to the the beam axis.

Following Deutschmann et al.[12,13] a parameter λ was introduced to allow for possible deviations from ideal, random-phase, non-interacting bosons, giving the correlation function that was used in this analysis:

$$C_2(\mathbf{p}_1, \mathbf{p}_2) = 1 + \lambda\exp\left\{-\left(\frac{q_\perp^2 R_\perp^2}{2}\right) - \left(\frac{q_\parallel^2 R_\parallel^2}{2}\right) - \left(\frac{q_0^2 \tau^2}{2}\right)\right\} . \tag{7}$$

The parameter λ in Eq. 7 has been given this interpretation: if $\lambda = 1$, the source is fully incoherent, and if $\lambda = 0$, the source is fully coherent. An example of a second-order coherent[14] source is a laser. The effect of lasing on λ depends on the event-mixing method, and emphasizes the assumption that the events have similar momentum distributions to each other. If the laser always has the same orientation, event mixing produces a true reference sample and $\lambda = 0$. If the laser changes orientation randomly from one event to the next, the correlated momentum-difference spectrum will remain a δ-function. However, the reference

sample calculation will mix pions of random orientation and will be uniform. The ratio will then be a δ-function, and λ will be large (possibly larger than one).

It has been proposed that under suitable conditions coherent emission of pions could take place,[15,16] similar to a laser, and measurements of λ might be able to detect this. In addition to the difficulties given above, lasing is not the only mechanism that can influence the value of λ. Final-state interactions of the pions can reduce the value of λ, with the amount of reduction depending also on the source size. Calculations of the strong-interaction effect for Ar + KCl give λ in the range of 0.8–0.9, and the value will be closer to one (the effect will decrease) for larger systems.[17] Decay of resonances and dynamical correlations can also influence the value of λ.[18]

In the above discussion, dynamical correlations influence the value of λ through the assumption that $\rho(\mathbf{x}, t)$ has no momentum dependence. More complete derivations of correlation functions can be found in Gyulassy,[18] Hama and Padula,[8] and Pratt.[3] A momentum-dependent source could arise in isotropic emission in the local rest frame of an extended, expanding source. Pratt[7] has shown that such a source would give an apparent source size that would decrease as a function of the pion energy, because of the correlation between the average pion energy and the emission point. As a result, he suggested[19] that measuring a pion source that increased in size when the average pion momentum was increased (through momentum cuts) would be a signature of an expanding source.

C. The Experimental Correlation Function

The experimental correlation function is defined to be the ratio of the two-particle cross section to two single-particle cross sections by

$$C_2(\mathbf{p_1}, \mathbf{p_2}) = \mathcal{D} \frac{d^6\sigma/dp_1^3 \, dp_2^3}{(d^3\sigma/dp_1^3)(d^3\sigma/dp_2^3)} , \tag{8}$$

where $\mathcal{D}$ is a normalization constant, $d^6\sigma/dp_1^3 \, dp_2^3$ is the two-pion inclusive cross section, and $d^3\sigma/dp^3$ is the single-pion inclusive cross section. In nuclear collision experiments, the single-pion cross sections (the reference sample) are usually estimated from the relative momentum spectrum of like-sign pions from different events (known as event mixing). The reasons for using event mixing are outlined below:

- Using unlike-sign pions has the difficulty that the different detection efficiencies for pions of different signs are not accurately known and will distort the measured correlation function.

- Generating the reference sample from theoretical models has the difficulty that nuclear collisions are not understood well enough to predict what the two-particle momentum spectra would be in the absence of Bose-Einstein effects.

- Simply measuring the single-pion momentum spectrum has the difficulty that the number of pions produced in the nuclear collision depends on the impact parameter. Therefore, a two-pion trigger is biased towards more central collisions than a one-pion trigger.[20] The only way to properly reproduce the bias is to require that the track-finding routines find two tracks in an event and then to ignore one of the tracks—which is the basis of the event-mixing method.

Event mixing does not completely remove the effects of the Bose-Einstein correlation. In this analysis the residual correlation effect was removed from the

reference sample by weighting the events as in Zajc *et al.*,[20] with the improvement that for each set of correlation function parameters the weighted events were used iteratively to approximate the true one-particle momentum spectrum needed to calculate the event weights. The converged event weights were then used to find the correlation function which was fit to find new parameters. As before, the correlation function parameters are then iterated until stable against further iteration. The calculation is shown in detail in Appendix A.

D. The Coulomb Corrections

The Coulomb interactions of the pions with each other and with the nuclear fragments have to be taken into account. The pion-nuclear matter interaction was handled by correcting the individual pion momentum before histogramming. The nuclear collision was simplified by assuming that there are three regions of nuclear matter after the collision—the target fragment (at rest in the laboratory), the interaction region (at center of mass rapidity) and the projectile fragment (at beam rapidity). The assumed charge distribution in these regions was 20%, 60%, and 20%, respectively, as calculated for an average impact parameter.[21] Note that the averaging included the impact-parameter biasing caused by the spectrometer's acceptance for two-pion events. The momentum-correction formula used was taken from Gyulassy and Kauffmann.[22] The temperatures of the nuclear matter in the fragments were taken from Nagamiya *et al.*,[23] Hayashi *et al.*,[24] and Sullivan *et al.*[25] The pion-pion interaction was handled by weighting the reference sample events with the Gamow factor[26] to reflect the probability of detecting a pion pair produced with a given momentum difference.

E. Fitting the Correlation Function

The correlation function was fit by using the maximum-likelihood method to maximize the agreement in the three-dimensional histograms of the equation

$$R_{ijk} = D \cdot C_{ijk} \cdot B_{ijk} , \tag{9}$$

where R_{ijk} is the correlated momentum-difference spectrum (the subscript ijk means that the quantity is evaluated at the ijk-th histogram bin), B_{ijk} is the reference sample momentum-difference spectrum, D is a normalization constant, and C_{ijk} is the correlation function defined as in Eq. 7, giving fitting parameters D, λ, $R_{\perp}$, $R_{\parallel}$, and τ. The R_{ijk} were assumed to be distributed with Poisson statistics, and the B_{ijk} were assumed to have negligible statistical fluctuations compared to the R_{ijk}. The fit was then made by adjusting the parameters to maximize the product over all bins of the probability of measuring R_{ijk}, assuming the predicted number of counts to be $D \cdot C_{ijk} \cdot B_{ijk}$ with a Poisson distribution.[20,27] Two estimators of the quality of the fit were used in this analysis. The first was a restricted χ^2 and the second was the χ^2_{PML}, as defined below.

The χ^2 was calculated in the usual manner, except that only those bins predicted to have more than five counts are used.[28] Although the correlated momentum-difference spectrum was assumed to be Poisson distributed, for more than five counts per bin the Poisson distribution is essentially identical to the Gaussian, and the χ^2 calculation applies. The distribution of the restricted χ^2 is that of a true χ^2 with the number of degrees of freedom (NDF) in the range of $N - L$ to N, where N is the number of bins used, and L is the number of parameters in the fit.[28] The number of degrees of freedom reported here is always $N - L$. This estimator has the virtue of allowing confidence levels to be estimated using

9

standard methods, and has the failing of not being sensitive to the entire region being fit.

The χ^2_{PML} was derived from the maximum-likelihood fitting method and was calculated from the formula of Zajc *et al.*[20] The parameters were fit by minimizing the quantity $F = -\ln\Phi$ (where Φ is the likelihood function). The related quantity, $\chi^2_{\text{PML}} = 2F + (\text{constant})$, has the additional property that it reduces to the usual χ^2 when the number of counts per bin is large. Explicitly showing the constant, the expression is

$$\chi^2_{\text{PML}} = -2\sum_{i,j,k}\ln\left\{\frac{(D\cdot C_{ijk}\cdot B_{ijk})^{R_{ijk}}}{R_{ijk}!}e^{-D\cdot C_{ijk}\cdot B_{ijk}}\right\} - \sum_{i,j,k}\ln\left\{2\pi R_{ijk}\right\} , \quad (10)$$

where the sums are restricted to bins where $B_{ijk} \neq 0$. Although this estimator is unbiased even if the number of counts per bin is small, it has the difficulty that its distribution is not known.[29] This estimator has the virtue of being sensitive to the entire region being fit and the failing of not allowing confidence levels to be calculated.

F. A Summary of Parameter Fitting

The iteration scheme for extracting the parameters using event weights in its entirety is: (1) Assume values for the parameters typical of nuclear size and use these to calculate $C(\mathbf{p_1}, \mathbf{p_2})$ with Eq. 7. (2) Iterate the event weights until stable against iteration (see Appendix A for details). (3) Make a set of new, more accurate, parameters for $C(\mathbf{p_1}, \mathbf{p_2})$ by using Eq. 9 and fitting to Eq. 7 with the maximum-likelihood method. (4) Use the parameters from the fit in step (3) to start again in step (1), iterating (1) to (3) until stable. In Monte Carlo tests, it was verified that this scheme gives values for parameters which were within the statistical uncertainties of the input values. Convergence was obtained in about

10

five iterations.

III. APPARATUS

The heavy ion beams for this experiment were provided by the Bevalac accelerator at Lawrence Berkeley Laboratory to beam line 30–2. The parameters for the beams used are given in Table I.

The Janus spectrometer, shown in plan view in Fig. 1, consisted of two dipole magnets, a "C" magnet near the target and the "Janus" window-frame magnet. Between the C magnet and the Janus magnet were two wire chambers, and after the Janus magnet were two more wire chambers. The wire chambers each consisted of three sense-wire planes with a 2 mm wire spacing. There were also a number of scintillation counters for triggering, time-of-flight determination and energy-loss measurement. Figure 1 shows the spectrometer as used in the Nb and Ar runs. For the earlier Fe runs, part of the lead shielding wall between the second wire chamber and the beam line was absent, and a different second wire chamber was used. The spectrometer is described in greater detail by Chacon.[27]

The target materials used in this experiment are given in Table II. The target holder rested on the lower pole tip of the C magnet. Therefore, the target used in the 0° Fe runs was stainless steel,[30] since the target could not be magnetic when the C magnet is used. Targets 0.5 to 1.0 gm/cm^2 thick were used in all cases as a compromise between event rate and multiple scattering or secondary interactions.

A source of primary interactions other than the target was expected to be the air near the target. This effect was expected to be largest in the 0° configuration since the target traceback information was less useful for determining the location of the interaction when the angle between the beam and the pion pairs was small.

The target was removed for some of the data-taking runs and the data were analyzed for tracks in the same fashion as the real data. The ratios of pion pairs found per beam particle with the target in to that with the target out are given in Table II. In the worst case the ratio is approximately 10:1. Note that for Nb in the 45° configuration the ratio is much higher than in the 0° configuration, as expected.

The acceptance of the spectrometer for the Fe setup is given on a $p_\perp$ vs. rapidity plot in Fig. 2. The data shown are Monte Carlo data, with one track per event, weighted to reflect the particle emission probability (the invariant cross section had a slope parameter of 100 MeV).[23,24] The figure contains both the 45° and the 0° configurations. The contours are linearly spaced with an arbitrary normalization and each of the acceptances contains the same number of counts. For the other systems, the magnetic fields in the spectrometer were adjusted to keep the acceptance in the same position relative to the center-of-mass velocity for the 45° configuration and relative to the projectile-fragment velocity for the 0° configuration. Table III gives the corresponding spectrometer characteristics.

The trigger for the data-collection hardware was the coincidence between the two scintillation counters in front of the Janus magnet, two of the pairs of scintillation counters (referred to as the AB array) after the last wire chamber, the prompt signal from any plane of the first wire chamber and the prompt signal from any two of the three planes in each of the remaining wire chambers.

Once the event was triggered, the data were acquired using CAMAC modules, read out by a program running on a micro-programmable branch driver (a Bi Ra MBD–11) connected to a PDP–11/45 (for the Fe data) or a VAX–11/750 (for the Ar/Nb data). The PDP–11/45 based system could acquire approximately 200

events during the one-second beam spill at 100% dead time whereas the VAX–11/750 based system could acquire approximately 300 events per spill at 50% dead time. The data-acquisition software was the Q system.[31]

IV. ANALYSIS

A. Hit and Track Finding

Each particle passing through a wire chamber usually fired a wire in each of the three planes of wires. Because of finite wire resolution and parallax, the three wires do not appear to pass through a single point but instead defined a small triangle. By taking all possible combinations of one wire from the fired wires in each of the planes, and calculating the size of the triangle formed, it can be determined if the triplet of wires should be associated with a single particle's passage through the wire chamber. So the size of the triangle formed by each triplet of wires in the wire chambers was calculated and, if less than a maximum size, the triplet of wires was considered a possible hit.[27] The triangles were then ordered by size, and those triangles that did not share wires with smaller triangles were considered to be valid hits. Any wires that were not yet associated with hits were checked to see if they cross within the chamber boundaries, and these were also considered to be valid hits. The locations of the hits were then passed to the track-finding routine. To allow the track finding to proceed at a reasonable pace, the motion of the particles in the magnetic fields was handled in the effective edge approximation, with vertical focussing.[20,27,32]

The accuracy of track finding has two aspects. The first is the efficiency for finding single tracks, and the second is the efficiency for finding the two tracks correctly. The track finding in single-track and double-track events was studied

with Monte Carlo data made using the magnetic field map with simulated multiple scattering and energy loss. The major concern here was that the two-track efficiency must depend in a predictable way on the event geometry, so it can be simulated in the reference sample.

There were three possible results of using the track-finding routine on the data from a Monte Carlo event: first, the two tracks in the event can be found correctly; second, the event can be missed because not enough tracks can be found; third, the event can be returned with the tracks confused—that is, with some hits from different tracks incorrectly assigned. Monte Carlo studies showed that for hit separations of greater than 2 cm, tracks were not confused, and the fraction of correctly found events was approximately constant.[27]

B. Two-Track Efficiency Simulation

The hardware and track-finding software influence the two-track efficiency, which had to be simulated in the reference sample using the event geometry. The requirements that were imposed on the real data, so that the two-track efficiency was well defined, were also imposed on the reference sample and were also used when calculating the event weights.

First, there was the hardware trigger requirement. Since the triggering requirement was that two independent AB counter pairs fire, the two tracks were required to trace to different AB counter pairs for the event to be accepted. Second, the requirement that triangles not share wires reduced the detection probability for two hits that do share wires. Thus, the hits in a pair of tracks were required to be such that, if all planes fired, the separation of the wires in all planes was greater than or equal to 3.5 wires.[27] Third, the effective-edge track reconstruction

14

misassigned hits in a pair of tracks about 40% of the time when the hits were separated by less than 2 cm, so the two tracks were required to be separated by at least 2 cm in all wire chambers.

C. Track-Parameter Fitting

The tracks' parameters (e.g., the initial momentum and the position at the target) were calculated as functions of the wire numbers. These were obtained from Monte Carlo simulation of a large number of tracks produced while varying the initial position of the particle and its vector momentum. Each desired parameter was then fit with a principle component analysis,[33] using orthogonal polynomials as a function of the five most significant wire number combinations. In this analysis Chebyshev polynomials were used, since these minimize the error when interpolating data.[34]

Monte Carlo data with multiple scattering and energy loss were used to determine the momentum resolution of this procedure, and the results are given in Table IV. The coordinate system used is: $\hat{x}$ is perpendicular to the beam (towards Janus), $\hat{y}$ is opposite to the beam direction and $\hat{z}$ is vertical. To determine the momentum-difference (q) resolution, two-track Monte Carlo events were used. From the data of Table IV, the resolution in the components of the momentum-difference histogram are computed to be $\Delta q_0 = 2$ MeV, $\Delta q_{\parallel} = 2$ MeV/c, and $\Delta q_{\perp} = 7$ MeV/c. Note that p was calculated in the laboratory frame and q was calculated in the nucleus-nucleus center-of-mass frame. The spectrometer's resolution is estimated to change the value of the correlation function (by broadening the correlation function) in any of the bins of the histogram by less than 1% (FWHM).

The four-momentum differences were histogrammed over a range of 0–250 MeV/c (or MeV for q_0) with a bin width of 10 MeV/c (or MeV). This gives a range of approximately 1 to 20 fm (or fm/c) over which $R_\perp$, $R_\parallel$, and τ were resolvable.

D. Particle Identification

When the spectrometer was set to accept negative particles, all detected particles were assumed to be negative pions. Particles not originating near the target were eliminated by the target-traceback cuts. The electron contamination of particles coming from the target was estimated by using the π°/π^- ratio, as predicted by isospin conservation, and using the branching ratios of $\pi^\circ \to 2\gamma$ and $\pi^\circ \to \gamma + e^+e^-$. The conversion probability for the γ's in the target and the air up to the first counters was calculated. The assumption was made that the electrons have the same momenta as the π°, which will overestimate the number of electrons in the range of momentum accepted. The electron contamination was estimated to be less than or equal to 5% of the total data sample.

V. RESULTS

A. Presentation of the Data

The data were histogrammed and fit as a function of $q_\parallel$, $q_\perp$, and q_0. Attempting to display the fit by fixing two of the variables and showing the data as a function of the third would produce 25×25 such displays and most of the bins in any display would be empty, both from the acceptance limits of the spectrometer, and the physical constraint that $q_\parallel^2 + q_\perp^2 \geq q_0^2$. For graphical display of the data and the fitted correlation function, one variable was retained, and an average was

16

made over the remaining variables. Three displays were made by using each of the three variables ($q_\parallel$, $q_\perp$, and q_0) in turn. Note that these averages are weighted by the spectrometer's acceptance in momentum-difference space.

More precisely, the definition of the data points in the k projection (denoted C_k) is

$$\mathcal{C}_k = \frac{\sum_{i,j} R_{ijk}}{D \cdot \sum_{i,j} B_{ijk}} \, , \tag{11}$$

the uncertainty in the data points is estimated as

$$(\Delta \mathcal{C}_k)^2 = \mathcal{C}_k^2 \left\{ \frac{1}{\sum_{i,j} R_{ijk}} + \frac{\sum_{i,j} (\Delta B_{ijk})^2}{\sum_{i,j} (B_{ijk})^2} \right\} \tag{12}$$

and the fitted curve is given by

$$\langle C_k \rangle = \frac{\sum_{i,j} C_{ijk} \cdot B_{ijk}}{\sum_{i,j} B_{ijk}} \, , \tag{13}$$

where (as in Eq. 9), D is a normalization constant, R_{ijk} is the correlated momentum difference spectrum (for the ijk-th histogram bin), B_{ijk} is the reference sample momentum difference spectrum, C_{ijk} is the value of the fitted correlation function, and ΔB_{ijk} is the estimated uncertainty in B_{ijk} (see Appendix A). Note that, if $R_{ijk} \approx D \cdot C_{ijk} \cdot B_{ijk}$, the curves will be close to the data points. From Eq. 13 one can see how the averages are weighted by the spectrometer's acceptance.

B. Fits to Monte Carlo Data

A Monte Carlo test of the fitting routines was made to verify their accuracy and to account for any distortions induced by the spectrometer's acceptance. The data for the test were generated so that the pion correlation function was given by Eq. 7, with $\lambda = 1$, $R_\parallel = 3$ fm, $R_\perp = 4$ fm, and $\tau = 2$ fm/c, these being typical

of the values expected for the fits to the real data. The Monte Carlo pions were then processed by simulating the spectrometer as used in the $0°$ Nb setup. The data output from the simulation were passed to the usual data-analysis stream with the usual geometrical cuts. The only difference was that the pulse-height and time-of-flight cuts in the scintillation counters were not used since particle contamination was not simulated. This procedure gives a close approximation to the spectrometer's momentum acceptance limits and two-track efficiency effects.

Table V gives the parameters extracted from the fit to the Monte Carlo data. The confidence level for this fit (based on the χ^2/NDF) is 55%. In Figure 3 the projections for this fit and the corresponding confidence contours are shown. In the projections some effects of the spectrometer's acceptance can be seen: First, the intercept as $q \rightarrow 0$ is not $C_2 = 1 + \lambda$ as one might expect from Eq. 7. Second, the shapes of the data and the fitted curves do not follow Eq. 7, most obviously for $q_{\parallel}$. However, the projections for both the data and the fitted correlation function have the same shape, indicating that these are acceptance weighting effects.

The kinematic relation $Q \cdot (P_1 + P_2) = 0$ (where P_1 and P_2 are the four momenta of the two pions and $Q = P_2 - P_1$) implies that $\mathbf{q} \cdot \boldsymbol{\beta}_{\pi\pi} = q_0$ (where $\mathbf{q} = \mathbf{p}_2 - \mathbf{p}_1$, $q_0 = E_2 - E_1$ and $\boldsymbol{\beta}_{\pi\pi} = (\mathbf{p}_1 + \mathbf{p}_2)/(E_1 + E_2)$ is the velocity of the center of mass of the pions); Thus there is a coupling between the radius parameter parallel to the average of $\boldsymbol{\beta}_{\pi\pi}$ and the lifetime parameter.[3] In this spectrometer, the average direction of $\boldsymbol{\beta}_{\pi\pi}$ is determined largely by the direction of the acceptance and is approximately parallel to the beam direction in the $0°$ acceptance and perpendicular to the beam direction (in the center of mass) in the $45°$ acceptance. In the confidence contour plots a coupling between two variables causes the principal axes of the confidence contour ellipse to not be parallel to the coordinate

axes. Instead, the axes are parallel to whatever combinations of the variables are independent. In the confidence contour plots for the Monte Carlo data one can see a somewhat greater coupling between $R_\parallel$ and τ, than between $R_\perp$ and τ. The Monte Carlo was a simulation of the $0°$ spectrometer where this was expected.

A spectrometer with a large angular acceptance will collect a significant fraction of the data at values of $\mathbf{q}$ too large to be useful for the determination of the shape of the correlation function. This is particularly true where the full event is reconstructed. In the projections one can see that the statistical uncertainties of the data points are approximately equal (for q_0 or $\mathbf{q}$ less than approximately 150 MeV or MeV/c), showing that the acceptance of the Janus spectrometer is sufficiently biased towards low $\mathbf{q}$ to offset the phase-space effect, giving a good determination of the correlation function for the data samples used.

C. Study of the Momentum Dependence of the Parameters

The dependence of the parameters on the pion momentum was studied by imposing cuts on its magnitude. For the $45°$ data, these cuts were made on the momentum measured in the nucleus-nucleus center of mass (denoted $\mathbf{p}_{cm}$). To remove improperly reconstructed tracks, both pions were required to have a momentum in the center of mass greater than the lower limit of the acceptance of the spectrometer. The value of this cut was 90 MeV/c for the Ar data, 100 MeV/c for the Fe data and 110 MeV/c for the Nb data. In Fig. 2, the cut for the Fe data is indicated by the curve marked "A" superimposed on the $45°$ data. In the second set of fits for the $45°$ data, the cut was increased to $|\mathbf{p}_{cm}| > 150$ MeV/c. In Fig. 2, this cut is indicated by the curve marked "B" superimposed on the $45°$ data.

19

For the 0° data, the reference frame was changed from the nucleus-nucleus center of mass to a reference frame moving with the projectile's velocity, since the projectile fragment was the nuclear matter with the smallest velocity relative to the pions and, therefore, the largest Coulomb correction. The 0° data samples have $|p_{proj}| > 50$ MeV/c, where p_{proj} denotes the momentum in the projectile frame. This requirement removed the pions with the largest Coulomb correction. In Fig. 2 this cut is indicated by the curve marked "A" that is superimposed on the 0° data. For the second set of fits for the 0° data the value of the cut was changed to $|p_{proj}| > 100$ MeV/c, which removes about one half of the pion pairs. In Fig. 2 this cut is indicated by the curve "B" superimposed on the 0° data. Note that although these cuts were made in the projectile frame, the correlation functions for all data sets were calculated in the nucleus-nucleus center-of-mass frame.

These cuts define, for each of the configurations, a full data set and a smaller subset. The full data set in the 45° configuration will be called "uncut" since no properly reconstructed tracks were removed. In the 0° configuration the largest data set will be called the "least-cut" data set since the smallest number of tracks (for this configuration) were removed. The data sets which have had the momentum cuts raised to explore the momentum dependance of the source parameters will be called the "most-cut" data sets.

To better test the possibility of the pion-source size depending on the momentum of the pions, cuts were made on the average of the momentum of the two pions detected, $\langle p \rangle = (p_1 + p_2)/2$, where p_1 and p_2 are measured in the nucleus-nucleus center of mass. The 0° Nb data were divided into two independent data sets of roughly equal size, the first with $|\langle p \rangle| < 225$ MeV/c, and the second

with $|\langle p \rangle| > 225$ MeV/c (the range for $|\langle p \rangle|$ was approximately 100 MeV/c to 500 MeV/c). The 45° Nb data were divided into two similar data sets (although here the range for $|\langle p \rangle|$ was approximately 100 MeV/c to 650 MeV/c). These cuts were made to test the theoretical prediction[7] that an expanding source would give an apparent source size that decreases with increasing pion momentum.

D. Projections and Confidence Contours for the Data

Figure 4 shows the projections for the uncut and least-cut data samples of the Nb data for the two configurations. The left column shows the projections for the 0° Nb data sample with $|p_{proj}| > 50$ MeV/c. This data sample was chosen for display since it is the largest data sample and, therefore, has the smallest statistical uncertainty. These plots do not show any systematic differences between the data and the correlation function used to fit the data. Note the similarities between the 0° data and the Monte Carlo. For comparison, the projections of the 45° Nb data sample with $|p_{cm}| > 110$ MeV/c are shown in the right column. This is a slightly smaller data set, but again, no systematic differences between the data and the fitted correlation function can be seen. There are some systematic effects that could be masked in the projections. For example, bins along the line given by $q_0 = q_{||} = q_\perp$ could be high, and this would not be apparent in the projections. However, confidence levels calculated from the χ^2/NDF are verified to be acceptable.

Figure 5 shows the confidence contours for the Nb most-cut data samples. These data samples were chosen since they have the largest statistical uncertainties of the Nb samples. The left column shows the confidence contours for the fit to the 0° Nb data sample with $|p_{proj}| > 100$ MeV/c, and the right column shows the

confidence contours for the 45° Nb data with $|p_{cm}| > 150$ MeV/c. The shapes of the contours are typical of the contours for all of the data sets, although, for the data sets with fewer events, the error contours can intersect zero. Note that for the 0° data, $R_{\parallel}$ is more correlated with τ than is $R_{\perp}$. For the 45° data the situation is reversed, consistent with the explanation of this as being due to changing the orientation of the acceptance.

E. Study of the Coulomb Corrections

The corrections due to Coulomb interaction between the pions and the nuclear matter, and the interaction between the two pions (made using the Gamow factor), have been mentioned. In principle one has to solve the n-body interaction problem to determine the corrections exactly. To verify that the assumption that the interactions can be separated is acceptable for the acceptances used, fits were made systematically including and excluding each of the two corrections.[9] Based on this test it is concluded that the corrections may be calculated separately if, in the 0° data, $|p_{proj}| > 50$ MeV/c.

To further examine the Coulomb corrections, a data sample of π^+ pairs was taken in the 0° Nb configuration. Protons in the π^+ data sample were rejected by setting requirements on the time of flight and the energy loss in the scintillation counters. The proton contamination in π^+ data set was estimated to be 25%.[27] The small data sample size did not allow further reductions in the proton contamination.

F. Additional Uncertainties

The major source of systematic uncertainty was in the residual correlation calculation: the correlation function used as input was taken from the measurements

and was, therefore, uncertain. This effect was studied for both configurations. The statistical uncertainty followed by this uncertainty for the 0° Ar (least cut) and the 0° Fe (both cuts) data sets are shown in Table VI. Unless otherwise noted, the uncertainties shown remaining tables are the sum of the statistical uncertainty and the residual correlation calculation uncertainty.

G. The Pion-Source Parameters

Table VII and Figure 6 present the results for the 45° setup where the constraint to a spherical source, $R_\perp \equiv R_\parallel (= R)$, has been made. These fits are equivalent to the single-radius-parameter fits used earlier.[20,35,36,37,38] The projectiles and targets are as listed in Tables I and II. The data of Zajc et al.[20] are included on the Table because the acceptance of their spectrometer was similar to that in the current work. Note that Zajc et al. histogrammed (and fit) their data as a function of $q = |\mathbf{q}|$ and q_0, so the number of degrees of freedom there is quite different from this work. The results in this work agree with those of Zajc et al., within uncertainties.

Table VIII and Figure 7 present the results for the 45° data where $R_\perp$ and $R_\parallel$ are allowed to vary separately and the requirement on $|\mathbf{p}_{cm}|$ does not remove any (real) data. Table IX and Figure 8 show the results for the 45° setup as above, however, the requirement on the center-of-mass momentum of the pions was increased to $|\mathbf{p}_{cm}| > 150$ MeV/c. Examining the corresponding entries in Tables VIII and IX shows that, within the uncertainties, there is no dependence on the pion momentum. The 45° Ar data sample was too small to give statistically significant results in the second set of fits.

Table X and Figure 9 present results for the 0° setup with $|\mathbf{p}_{proj}| > 50$ MeV/c,

which is the least cut of the two sets of 0° fits. Table XI and Figure 10 show results for the 0° setup with $|\mathbf{p}_{\text{proj}}| > 100$ MeV/c. Note that, for the Fe and Nb data sets, the results agree within the uncertainties. For the Ar data the most-cut data are about two standard deviations smaller in all parameters. Table X also includes the parameters for the Nb π^+ data. The agreement between the π^- and the π^+ data is at the one standard deviation level for $R_\perp$, τ, λ and is considerably worse for $R_\parallel$. Unfortunately, the large proton contamination hampers making any definitive conclusions.

In the second test of the possibility that the pion-source size depends on the momentum of the pions, the 0° and 45° Nb data were divided into two data sets, $|\langle\mathbf{p}\rangle| < 225$ MeV/c, and $|\langle\mathbf{p}\rangle| > 225$ MeV/c. The parameters extracted from the fits to the 0° data are shown in Table XII. The parameters from fits to the 45° Nb data are shown in Table XIII. For the Nb data sets the radius and lifetime parameters agree within the uncertainties for these momentum cuts.

H. Discussion

Our work shows the pion source to be oblate or spherical ($R_\perp \geq R_\parallel$). Using a 4π streamer chamber, Beavis *et al.* have found spherical sources for 1.5 GeV/nucleon Ar + KCl with parameters[35] of $R_\perp = 5.0 \pm 0.5$ fm and $R_\parallel = 5.0 \pm 1.5$ fm (τ was fixed at 1.5 fm/c), and for Ar + Pb with parameters[37] of $R_\perp = 5.16 \pm 0.50$ fm, $R_\parallel = 5.76 \pm 0.54$ fm, and $\lambda = 0.98 \pm 0.14$ (for this fit, τ was fixed at 0.0). The Ar parameters are within one standard deviation of the parameters measured in the 0° Ar configuration in the current work, so the oblate shape obtained in the current work is within the uncertainties of the spherical shape obtained in the earlier work.

24

Using the HISS spectrometer at the LBL Bevalac, Christie[39] has measured the source parameters for 1.8 GeV/nucleon Ar + KCl (although with a different acceptance from either of the two acceptances in this work). His single-radius-parameter fit gives $R = 4.30 \pm 0.14$ fm, $\lambda = 0.78 \pm 0.05$ and $\chi^2/\text{NDF} = 745/726$, disagreeing with this work at the four standard deviation level. The parameter τ was fixed at 0.0 fm/c for his fit. His two-radius-parameter fit to the same system gives $R_\perp = 4.39 \pm 0.15$ fm, $R_\parallel = 3.48 \pm 0.30$ fm, $\tau = 1.3^{+0.90}_{-1.30}$ fm/c and $\lambda = 0.77 \pm 0.05$, with $\chi^2/\text{NDF} = 2088/2081$. His radius parameters are slightly smaller than the parameters measured in the 0° Ar configuration of the current work (approximately one standard deviation for $R_\perp$ and two standard deviations for $R_\parallel$), and the remaining parameters agree at the one standard deviation level. However, comparisons are complicated by the restriction of $\tau = 0.0$ fm/c in Christie's single-radius-parameter fit.

In the Plastic Ball at the LBL Bevalac, Bock et al.[38] found, for Nb + Nb at 650 MeV/nucleon, $R = 3.4 \pm 0.4$ fm (with τ fixed at 0.0 fm/c and $\chi^2/\text{NDF} = 1.5$)—a value one standard deviation different from the value in this work. The single-radius-parameter Ar + KCl fit of Beavis et al.[35,36] gives $R = 4.7 \pm 0.5$ fm, $\tau = 4.2^{+1.8}_{-4.2}$ fm/c and $\lambda = 1.2 \pm 0.2$. There is some disagreement between the numbers reported by Beavis et al. and the current work.

The parameters for the 45° configuration data in this work do not show any dependence on the pion momentum in the center of mass, and the parameters for the 0° configuration do not show any dependence on the projectile-frame momentum. The results for the different $|\langle \mathbf{p} \rangle|$ ranges also agree within the uncertainties. Therefore, the results do not show any evidence for collective expansion effects.[7,8] Beavis et al.[37] have also searched for collective expansion effects with cuts on

the average pion momentum, but the size of their data sample did not allow any definitive conclusions. Bock et $al.$[38] analyzed their Nb + Nb data, and Christie[39] analyzed his Ar + KCl data for variations in the source size as a function of the pion momentum, but each observed changes in the radius parameter at only the one standard deviation level, again not showing significant evidence for expansion.

A comparison of the 45° and the 0° ($|\mathbf{p}_{proj}| > 50$ MeV/c) results shows the pion source to be more spherical for the 0° data. The $R_\perp$ parameters for the two measured angular acceptances agree within the uncertainties, (comparing system by system); $R_\parallel$ is consistently smaller in the 45° configuration.

Considering the parameters as a function of A, for both configurations, $R_\perp$ shows only a weak dependence, increasing slightly with A. Within the uncertainties, $R_\perp$ could be independent of A. In the 45° configuration the source is oblate for the light system, becoming less so for the heavier systems. In the 0° configuration the source shape is slightly oblate, becoming spherical with increasing A. The τ parameter increases with A in the 45° configuration (although the statistical uncertainties are large); for the 0° configuration this effect is not as clear.

The λ parameter is less than one for the 45° configuration, for all systems, increasing slightly with A. The 0° configuration results show similar behavior, but the values are slightly larger, being just below one for Ar and just above one for Nb. A qualitative prediction has been made that λ will increase with source size (becoming closer to one) due to the strong interaction between the pions.[17] The results given here have not been corrected for the strong interaction, so the change in λ may be due to this effect. Comparisons of Tables VII and VIII show that restricting the source shape to spherical leaves λ unchanged and increases

26

the extracted τ by more than one standard deviation.

Figure 11 shows the parameter R_{rms} as a function of the atomic mass of the projectile (A_p) to the one-third power.[40] This Figure contains results from a range of energies, impact parameters and asymmetries (although the projectile was always lighter than the target). The experimental conditions and the references are listed in Table XIV. The radius parameters measured in the current work have been multiplied by $\sqrt{3/2}$ to give the RMS radius parameters used in the Figure and Table. Note that the results of the present measurement of the radius parameter are generally smaller than the prior measurements and show some increase with projectile mass. However, comparisons are hampered by the treatment of τ which is often fixed at some value.

There are two sets of results that can be compared with theory: those of the Ar single-radius-parameter fits and the Fe two-radius-parameter fits (see Tables VII and XVI). The calculations are taken from Humanic[46] and were made using the program CASCADE.[47] The measured R is much smaller than the calculation, and τ is larger. It is unclear if τ being larger is an artifact of fitting a restricted form of the correlation function, since restricting the form of the fitted correlation function to a single radius parameter causes τ to increase. The measured values of λ are smaller than the predicted values.

A comparison of the Fe results and CASCADE calculations has been published earlier.[9] The calculated sizes are generally larger and less oblate than the measured values. In the absence of theoretical results, one can speculate as to what effects the modifications of the theories will have on the calculated parameters. The inclusion of nucleon-nucleon repulsion terms (which CASCADE lacks) will make the interaction region larger, because the nucleons will resist compression, and will

27

reduce the energy density in the collision. The repulsion will also cause energy to be stored as compressional energy. These two effects would decrease the energy density available for pion production. Assuming that the energy density in the nuclear collision is near the pion production threshold, this could decrease the pion-source size, since the energy density in the outer regions of the collision would drop below the production threshold. If nuclear repulsion is present in nuclear collisions, and if the energy density is near the pion production threshold, then the measured source size could be smaller and longer lived than the CASCADE result.

A repulsion term will expand the source perpendicular to the beam axis, since the increased pressure will push matter out the sides of the interaction region, giving sources that are more oblate than the CASCADE calculations. In Table XVI it can be seen that the measured sources are more oblate than the calculation, the measured $R_\perp$ being equal to or slightly larger than the prediction, while the measured $R_\parallel$ is smaller. Here, however, the measured lifetime is shorter than the CASCADE prediction. Collective flow will, to some extent, cause the momentum distribution of the pions to be peaked in the direction of the flow. This could cause the pion momenta to be correlated in addition to the Bose-Einstein symmetrization, and could lead to a measured λ smaller than the CASCADE prediction.

VI. SUMMARY

The method of pion-pion interferometry was used to measure the pion-source parameters for three target-projectile combinations, with two acceptances. The data analysis method has been verified by Monte Carlo simulations to give parameters that are within the statistical uncertainties of the values used as input.

The large data samples present in this experiment have allowed the determination of the pion-source radius perpendicular and parallel to the beam axis. The lifetime of the source was measured and, in the larger data sets (coincidentally, the heavier ions), was found to be non-zero. The source size perpendicular to the beam was approximately constant showing only a weak dependence on viewing angle and nuclear mass. The source size parallel to the beam increased with the nuclear mass, and was larger in the $0°$ configuration than the $45°$ configuration. The source size seemed independent of the average pion momentum.

For a systematic study of the deviation of the source size from an $A^{1/3}$ scaling further experiments would need to be done. Measurements (with equal-mass target and projectile to make comparisons easier) need to be made in the region of $A \approx 10$ and $A \approx 20$. Suitable choices for beams and targets are $^{12}C + C$ and $^{20}Ne + NaF$.

Further experiments would need to be done to study the dependence of the source shape on the atomic mass. Again, measurements need to be done for the lower atomic mass in the region of $A \approx 10$ and $A \approx 20$. Until the dependence of the source shape (or lack of it) on the energy of the collision is understood, these experiments should be done at a constant energy per nucleon. Existing data are consistent with a dependence of the shape on the beam energy (more spherical at lower energy per nucleon).

VII. ACKNOWLEDGEMENTS

APPENDIX A: MEASUREMENT OF THE CORRELATION FUNCTION THROUGH EVENT MIXING

In this appendix the effect of the pion correlation on the reference sample is calculated, and a method of eliminating the effect by weighting the events is given. The effect is first demonstrated in a simplified form, then the equations used in the analysis are given.

This experiment measures N two-particle events, where each event α ($\alpha = 1, 2, \ldots, N$) is defined by a momentum pair $(\mathbf{p}_{1\alpha}, \mathbf{p}_{2\alpha})$. Suppose that the momentum pairs are histogrammed into M bins for each momentum. Define a histogramming function δ_α^{ij} by

$$
\delta_\alpha^{ij} = \begin{cases} 1 \text{ for } \mathbf{p}_{1\alpha} \in i\text{-th momentum bin and} \\ \quad \mathbf{p}_{2\alpha} \in j\text{-th momentum bin.} \\ 0 \text{ otherwise.} \end{cases} \tag{A1}
$$

Then the number of counts in the (i, j) histogram bin is just

$$
N_{ij} = \sum_{\alpha=1}^{N} \delta_\alpha^{ij} . \tag{A2}
$$

Model the spectrometer by defining η_i to be the detection probability of a particle in bin i (where $\sum_i \eta_i = 1$), including both the emission probability (in the absence of Bose-Einstein effects) and the spectrometer's single-track efficiency; C_{ij} to be the value of the correlation function for bin (i, j); and ρ_{ij} to be the two-track contribution to the detector's efficiency. The probability of a particle pair in bin (i, j) being in the data sample is

$$\mathcal{P}_2(i,j) = A\eta_i\eta_j C_{ij}\rho_{ij} \ , \tag{A3}$$

where the normalization constant A is chosen so that $\sum_{i,j}\mathcal{P}_2(i,j) = 1$. On the other hand, the observed probability for the particle pair is

$$\mathcal{P}_2(i,j) = \frac{1}{N}\sum_{\alpha=1}^{N}\delta_\alpha^{ij} \ . \tag{A4}$$

In event mixing, the single-particle momentum spectrum is estimated by ignoring one of the two momenta in the event. For the sake of definiteness, the second momentum will be ignored here, but the choice is arbitrary. Define a histogramming function that ignores the second momentum by

$$\delta_\alpha^i = \begin{cases} 1 \text{ for } \mathbf{p}_{1\alpha} \in i\text{-th momentum bin.} \\ 0 \text{ otherwise.} \end{cases} \tag{A5}$$

The probability of detecting a single particle in momentum bin i, as determined by event mixing, can be written as

$$\mathcal{P}_1(i) = \frac{1}{N}\sum_{\alpha=1}^{N}\delta_\alpha^i \tag{A6}$$

$$= \frac{1}{N}\sum_{j=1}^{M}\sum_{\alpha=1}^{N}\delta_\alpha^{ij} \ . \tag{A7}$$

Equation A7 follows from Eq. A6 because the second particle's momentum is assumed to be in one of the momentum bins. Using Eqs. A3 and A4, Eq. A7 becomes

$$\mathcal{P}_1(i) = A\eta_i\sum_{j=1}^{M}\eta_j C_{ij}\rho_{ij} \ , \tag{A8}$$

and it can be seen that the event-mixing method, instead of giving η_i, the single-track detection probability, gives a value weighted by the correlation function and the two-track efficiency.

Setting

$$W_i = \left(\sum_{j=1}^{M} \eta_j C_{ij}\rho_{ij} \right)^{-1} , \tag{A9}$$

equation A3 becomes

$$\mathcal{P}_2(i,j) = A^{-1}W_i\mathcal{P}_1(i)W_j\mathcal{P}_1(j)C_{ij}\rho_{ij} , \tag{A10}$$

and the correlation function is

$$C_{ij} = \frac{A\mathcal{P}_2(i,j)}{W_i\mathcal{P}_1(i)W_j\mathcal{P}_1(j)\rho_{ij}} . \tag{A11}$$

So, by weighting the histogram bins, the effect of the correlation on the reference sample can be removed, and it is possible to measure the correlation function using event mixing.

Below is a successive-approximation scheme for the η_i. No proof of convergence is given beyond noting that, for the data sets in this experiment, the changes observed from one iteration to the next become small, and that in Monte Carlo tests the parameters returned are within the statistical errors of the input parameters.

Since $C_{ij}\rho_{ij} \approx 1$ on the average, it is expected that $\Delta_{ij} = C_{ij}\rho_{ij} - 1$ will be a small number. Substituting this into Eq. A8 gives

$$\eta_i = \frac{A^{-1}\mathcal{P}_1(i)}{\sum_{j=1}^{M}\eta_j + \sum_{j=1}^{M}\eta_j\Delta_{ij}} , \tag{A12}$$

and, using $\sum_i \eta_i = 1$, this becomes

$$\eta_i = \frac{A^{-1}\mathcal{P}_1(i)}{1 + \sum_{j=1}^{M}\eta_j\Delta_{ij}} . \tag{A13}$$

Since the Δ_{ij} are expected to be small, this result suggests the following scheme be used to find the detection probabilities: To first order assume that $\Delta_{ij} = 0$ or $\eta_i = A^{-1}\mathcal{P}_1(i)$ (where $\mathcal{P}_1(i)$ determined from Eq. A6) then calculate each succeeding order of η_i using the preceeding order in the right hand side of Eq. A13.

32

The normalization, A, can be found by using $\sum_i \eta_i = 1$ at each step. Note that Eq. A13 is used only to show that forcing the normalization of the η_i to be constant is equivalent to a successive-approximation scheme in the Δ_{ij}, the form used in the analysis follows. Prior experiments (e.g., Zajc et al.[20]) used the equivalent Eq. A13 only once, which was not sufficiently accurate for the current experiment.

The above bin-weighting scheme can be converted to an event-weighting scheme[27] by defining, for functions of the momentum bins, G_i, a function of the particle momentum, G_α, such that

$$G_i \sum_{\alpha=1}^{N} \delta_\alpha^i = \sum_{\alpha=1}^{N} G_\alpha \delta_\alpha^i \, , \tag{A14}$$

so that histogramming the weighted events is equivalent to weighting the histogram bins. Then the momentum histogramming assumed will not appear in the event-weight calculation and momentum-difference histogramming can be easily substituted in the analysis. In most cases the function will be unchanged, all that need be done is to evaluate the function using the momentum of the particle(s) in the event, not the center of the histogram bin. The resulting equations are shown here, using three-dimensional momentum-difference histograms as used in this analysis. First, define a histogramming function in analogy to Eq. A1 by

$$\delta_\alpha^{ijk} = \begin{cases} 1 & \text{for } (P_{1\alpha} - P_{2\alpha}) \in ijk\text{-th momentum} \\ & \text{difference bin.} \\ 0 & \text{otherwise.} \end{cases} \tag{A15}$$

The momentum difference spectrum for the particle pairs then is just

$$R_{ijk} = \sum_{\alpha=1}^{N} \delta_\alpha^{ijk} \, . \tag{A16}$$

In the event-weighting scheme, Eq. A6 becomes (using Eq. A14),

33

$$\mathcal{P}_1(\alpha) = \frac{1}{N} \ . \tag{A17}$$

Similarly, Eq. A8 becomes

$$\mathcal{P}_1(\alpha) = A\eta_\alpha \sum_{\beta=1}^{N} \eta_\beta C_{\alpha\beta}\rho_{\alpha\beta} \ . \tag{A18}$$

Using Eqs. A17 and A18, and solving for η_α gives

$$\eta_\alpha = \left(AN \sum_{\beta=1}^{N} \eta_\beta C_{\alpha\beta}\rho_{\alpha\beta} \right)^{-1} , \tag{A19}$$

where the condition that defines the normalization constant A becomes, in the event weighting scheme, $\sum_\alpha \eta_\alpha = 1$. The subscripts α and β are used to show that the quantities are evaluated using the momenta of the particles.

Modified event weights can be defined by $W'_\alpha = N\eta_\alpha$, so that Eq. A19 becomes

$$W'_\alpha = \left(\frac{A}{N} \sum_{\beta=1}^{N} W'_\beta C_{\alpha\beta}\rho_{\alpha\beta} \right)^{-1} , \tag{A20}$$

where it can be seen that the condition that defines A becomes $\sum_\alpha W'_\alpha = N$. The initial values for the event weights are $W'_\alpha \equiv 1$, with Eq. A20 being used to iterate the event weights in analogy to Eq. A13. Note that the modified event weights do not depend on the number of events in the data sample, unlike the η_α which scale as $1/N$.

The event weights that would be defined in analogy with Eq. A9 are

$$W_\alpha = \left(\sum_{\beta=1}^{N} \eta_\beta C_{\alpha\beta}\rho_{\alpha\beta} \right)^{-1} \tag{A21}$$

and give $W_\alpha = (AN)\eta_\alpha$, differing from the modified event weights only in the normalization. Since the overall normalization (in Eq. 9) is fit, the event weights are not calculated, and the modified event weights (Eq. A20) are used in the

reference-sample calculation (Eq. A23), thereby eliminating a step in the calculations.

Define a histogramming function for the event mixing in analogy with Eq. A15 using momenta from two different events

$$\delta_{\alpha\beta}^{ijk} = \begin{cases} 1 \text{ for } (P_{1\alpha} - P_{1\beta}) \in ijk\text{-th momentum} \\ \quad \text{difference bin.} \\ 0 \text{ otherwise.} \end{cases} \tag{A22}$$

As before, the arbitrary choice is made to use the first momentum in each of the two particle pairs. The reference sample, the denominator of Eq. A11 without the normalization factor, is then

$$B_{ijk} = \sum_{\alpha=1}^{N} \sum_{\beta=1}^{N} W'_\alpha W'_\beta \rho_{\alpha\beta} \delta_{\alpha\beta}^{ijk} . \tag{A23}$$

Because of the weighting factors, the statistical fluctuation in the bins is not just the square root of the number of counts. The estimated uncertainty in B_{ijk} is

$$(\Delta B_{ijk})^2 = 2 \sum_{\beta=1}^{N} \left\{ \sum_{\gamma=1}^{N} W'_\beta W'_\gamma \rho_{\beta\gamma} \delta_{\beta\gamma}^{ijk} \right\}^2 . \tag{A24}$$

Note that this gives $\Delta B_{ijk} \sim \mathcal{O}(N^{3/2})$. With $B_{ijk} \sim \mathcal{O}(N^2)$, the fractional error in the reference sample is $\Delta B_{ijk}/B_{ijk} \sim \mathcal{O}(N^{-1/2})$. This also can be written $\Delta B_{ijk} \sim \mathcal{O}(B_{ijk}^{3/4})$, as has been found earlier by other methods.[20] To reduce the fluctuations in the reference sample, all possible combinations of the particle momentum are used in the event mixing (Eq. A23).

The two-track efficiency, $\rho_{\alpha\beta}$, is estimated by imposing cuts based on the detector geometry using the data from the pion tracks in the events. The cuts are imposed on the two-track data to give a known $\rho_{\alpha\beta}$ which is then used in the event mixing and event weighting (in Eqs. A20 and A23).

The pion-pion interaction is handled by weighting the background events by the Gamow factor. This introduces a weighting factor in the calculation of the background that would be placed in Eq. A23 next to the $\rho_{\beta\gamma}$ term. This term is symmetric in the two pion momenta, and the derivation of the uncertainty in B_{ijk} follows the one used above. The pion-nuclear matter interaction is handled by correcting the individual pion's momentum before histogramming, which does not alter any of the derivations given.

REFERENCES

*Present address: Tektronix, P.O. Box 500, Beaverton, OR 97077.

†Present address: University of Pittsburgh, Pittsburgh, PA 15260.

‡Present address: Austrian Academy of Sciences, Boltzmanngasse 3, A–1090 Vienna, Austria.

§Present address: Physikalisches Institut der Universität Heidelberg, Philosophenweg 12, D–6900 Heidelberg, Germany.

‖Present address: Physik-Institut der Universität Zürich, Schönberggasse 9, CH–8001 Zürich, Switzerland.

¶Present address: Paul Scherrer Institut, CH–5234 Villigen, Switzerland.

**Present address: P2 Division, MS D456, Los Alamos National Lab., Los Alamos, NM 87545.

[1] A representative, but by no means complete, list of references is (in chronological order): J. Cugnon, T. Mizutani and J. Vandermeulen, Nucl. Phys. **A352**, 505 (1981); E. Braun and Z. Fraenkel, Phys. Rev. C **34**, 120 (1986); Y. Kitazoe, M. Sano, H. Toki and S. Nagamiya, Phys. Lett. **166B**, 35 (1986); C. Gale, G. Bertsch and S. Das Gupta, Phys. Rev. C **35**, 1666 (1987); D. Boal and J. Glosli, Phys. Rev. C **37**, 91 (1988); J. Molitoris *et al.*, Phys. Rev. C **37**, 1014 (1988); and J. Aichelin *et al.*, Phys. Rev. C **37**, 2451 (1988).

[2] S. Padula, M. Gyulassy and S. Gavin, Nucl. Phys. **B329**, 357 (1990).

[3] S. Pratt, Phys. Rev. D **33**, 1314 (1986).

[4] G. Bertsch, M. Gong and M. Tohyama, Phys. Rev. C **37**, 1896 (1988); G. Bertsch *et al.*, Phys. Rev. D **37**, 1202 (1988).

[5] G. Goldhaber, S. Goldhaber, W. Lee and A. Pais, Phys. Rev. **120**, 300 (1960).

[6] R. Hanbury-Brown and R. Twiss, Nature **177**, 27 (1956).

[7] S. Pratt, Phys. Rev. Lett. **53**, 1219 (1984).

[8] Y. Hama and S. Padula, Phys. Rev. D **37**, 3237 (1988).

[9] A. Chacon *et al.*, Phys. Rev. Lett. **60**, 780 (1988).

[10] A more complete derivation using a similar set of assumptions is given in M. Gyulassy, S. Kauffmann and L. Wilson, Phys. Rev. C **20**, 2267 (1979).

[11] W. Zajc, *Bose-Einstein Correlations—From Statistics to Dynamics* in **Hadronic Multiparticle Production**, editor P. Carruthers, World Scientific Press, 1988.

[12] M. Deutschmann *et al.*, CERN/EP/PHYS/78-1 (1978).

[13] M. Deutschmann *et al.*, Nucl. Phys. **B204**, 333 (1982).

[14] R. Glauber, Phys. Rev. Lett. **10**, 84 (1963); R. Glauber, Phys. Rev. **130**, 2529 (1963); R. Glauber, Phys. Rev. **131**, 2766 (1963).

[15] C. Lam and S. Lo, Phys. Rev. D **30**, 1336 (1986).

[16] M. Gulyassy, Nucl. Phys. **A354**, 395c (1981).

[17] M. Bowler, Z. Phys. C—Particles and Fields **39**, 81 (1988).

[18]M. Gyulassy, Phys. Rev. Lett. **48**, 454 (1982).

[19]S. Pratt (private communication).

[20]W. Zajc, Ph.D. thesis, University of California, Berkeley, 1982; Lawrence Berkeley Laboratory report LBL–14864 (unpublished); W. Zajc *et al.*, Phys. Rev. C **29**, 2173 (1984).

[21]The abrasion model, as outlined in L. Oliveira, Ph.D. thesis, University of California, Berkeley, 1978, Lawrence Berkeley Laboratory report LBL–8561 (unpublished), was used.

[22]M. Gyulassy and S. Kauffmann, Nucl. Phys. **A362**, 503 (1981).

[23]S. Nagamiya *et al.*, Phys. Rev. C **24**, 971 (1981).

[24]S. Hayashi *et al.*, Phys. Rev. C **38**, 1229 (1988).

[25]J. Sullivan (private communication); J. Sullivan *et al.*, Phys. Rev. C **25**, 1499 (1982).

[26]See, for example, E. Merzbacher, **Quantum Mechanics**, second edition, John Wiley & Sons, New York, 1970, pp. 245–249.

[27]A. Chacon, Ph.D. thesis, University of California, Berkeley, 1989; Lawrence Berkeley Laboratory report LBL–28149 (unpublished).

[28]A. Frodesen, O. Skeggestad and H. Tøfte, **Probability and Statistics in Particle Physics**, Universitetsforlaget, 1979.

[29]F. James, Comp. Phys. Comm. **20**, 29 (1980).

[30]The composition of the # 304 stainless steel target (as given by the supplier,

Castle Metals—A. M. Castle & Co.) was Fe: 70.9 %, Cr: 18.5 %, Ni: 8.5 %, Mn: 1.6 %, and Si: 0.5 % (by weight).

[31] J. Harrison et al., IEEE Transactions on Nuclear Science **NS–28**, 3724 (1981).

[32] A. P. Banford, **The Transport of Charged Particle Beams**, E. & F. N. Spon Ltd., London, 1966.

[33] H. Wind, *Principle Component Analysis and its Application to Track Finding*, in **Formulae and Methods in Experimental Data Evaluation** (Vol. 3), editors R. Bock et al., European Physical Society, CERN, Geneva, 1984.

[34] H. Wind, *Interpolation and Function Representation*, in **Formulae and Methods in Experimental Data Evaluation** (Vol. 3), editors R. Bock et al., European Physical Society, CERN, Geneva, 1984.

[35] D. Beavis et al., Phys. Rev. C **27**, 910 (1983).

[36] D. Beavis et al., Phys. Rev. C **28**, 2561 (1983).

[37] D. Beavis et al., Phys. Rev. C **34**, 757 (1986).

[38] R. Bock et al., Mod. Phys. Lett. A **3**, 1745 (1988).

[39] W. Christie, Ph.D. thesis, University of California, Davis, 1990; Lawrence Berkeley Laboratory report LBL–28986 (unpublished).

[40] J. Bartke, Phys. Lett. B **174**, 32 (1986).

[41] C. DeMarzo et al., Phys. Rev. D **29**, 363 (1984).

[42] G. Agakishiev et al., Sov. J. Nucl. Phys. **39** (3), 344 (1984).

[43] N. Akhababian, J. Bartke, V. Grishin and M. Kowlaski, Z. Phys. C—Particles

and Fields **26**, 245 (1984).

[44]S. Fung *et al.*, Phys. Rev. Lett. **41**, 1592 (1978).

[45]D. Beavis *et al.*, *Multi-Pion Production*, in **Proc. 7th High Energy Heavy Ion Study (Darmstadt, Oct. 1984)**, Report GSI–85–10 (Darmstadt, 1985) p. 771.

[46]T. Humanic, Phys. Rev. C **34**, 191 (1986).

[47]See Ref. 46 and references therein.

TABLE I. Beam parameters for the runs.

Ion	Kinetic Energy (GeV/nucleon)	Typical Intensity (Ions/Spill)	Beam Spot Size (cm)	Setups
^{40}Ar	1.82	$1 \cdot 10^8$	1×1.6	$0°$, $45°$
^{56}Fe	1.70	$1 \cdot 10^7$	1×6	$0°$, $45°$
^{93}Nb	1.54	$2 \cdot 10^7$	1×1	$0°$, $45°$

TABLE II. Spectrometer parameters for the setups used. The target In/Out ratio is the ratio of events found per beam particle with the target in to that with the target out. The uncertainty quoted is statistical only.

Setup	Target Material	Target In/Out Ratio	Magnet Fields C Magnet (kG)	Janus Magnet (kG)
Ar $0°$	KCl	33 ± 3	14.6	12.0
Ar $45°$	KCl	–	1.7	9.0
Fe $0°$	Stainless Steel	9.8 ± 0.2	14.2	11.4
Fe $45°$	Fe	–	0.0	8.6
Nb $0°$	Nb	15.6 ± 0.5	13.0	10.8
Nb $45°$	Nb	$103 ^{+28}_{-18}$	1.5	8.5

TABLE III. Spectrometer characteristics for the Fe setups.

θ_{lab}	θ_{cm}	$|p_{cm}|$ Accepted (MeV/c)	Solid Angle (msr)
$\approx 0°$	$0°$–$32°$	100–400	12
$\approx 45°$	$91°$–$106°$	100–600	29

TABLE IV. Resolution for Monte Carlo simulated events.

Quantity	RMS Error
p_x	3.6 MeV/c
p_y	2.2 MeV/c
p_z	3.4 MeV/c
q_x	5.1 MeV/c
q_y	1.7 MeV/c
q_z	4.8 MeV/c
q_0	1.8 MeV

TABLE V. Parameters extracted from Monte Carlo simulated events. Only statistical uncertainties are shown.

Parameter	Input Value	Fitted Value
$R_\perp(\mathrm{fm})$	4.0	3.8 ± 0.2
$R_\parallel(\mathrm{fm})$	3.0	3.2 ± 0.3
$\tau(\mathrm{fm/c})$	2.0	$2.2^{+0.6}_{-0.4}$
λ	1.0	0.98 ± 0.05
χ^2/NDF	–	595/600
$\chi^2_{\mathrm{PML}}/\mathrm{NDF}$	–	2646/2359
Events	–	14000

TABLE VI. Parameters with statistical uncertainties followed by uncertainties due to the residual correlation correction for the Ar and Fe $0°$ data sets.

| | Ar, $0°$ Data | Fe, $0°$ Data | |
	$\|\mathbf{p}_{\mathrm{proj}}\| > 50$ MeV/c	$\|\mathbf{p}_{\mathrm{proj}}\| > 50$ MeV/c	$\|\mathbf{p}_{\mathrm{proj}}\| > 100$ MeV/c
$R_\perp(\mathrm{fm})$	$4.8 \pm 0.3 \pm 0.07$	$4.8 \pm 0.2 \pm 0.05$	$4.7 \pm 0.3 \pm 0.08$
$R_\parallel(\mathrm{fm})$	$4.2 \pm 0.4 \pm 0.2$	$2.7 \pm 0.3 \pm 0.1$	$2.1 \pm 0.5 \pm 0.16$
$\tau(\mathrm{fm}/c)$	$1.1^{+1.4}_{-1.1} \pm 0.4$	$2.7 \pm 0.6 \pm 0.2$	$3.5 \pm 0.6 \pm 0.3$
λ	$0.81 \pm 0.05 \pm 0.03$	$0.88 \pm 0.03 \pm 0.015$	$0.75 \pm 0.05 \pm 0.02$
χ^2/NDF	$581/537$	$939/729$	$470/395$
$\chi^2_{\mathrm{PML}}/\mathrm{NDF}$	$2979/2590$	$2938/2420$	$1476/1300$
Events	$12{,}900$	$32{,}000$	$11{,}200$

TABLE VII. Parameters as a function of the projectile, for the $45°$ data. The data marked Ar (Zajc) are the Ar π^- data of Zajc et al.[20]; the remaining data are this work. Only statistical uncertainties are shown.

| | $45°$ Data, Single-Radius-Parameter Fit | | | |
Projectile	Ar (Zajc)	Ar	Fe	Nb
$R(\mathrm{fm})$	$2.77^{+0.6}_{-0.9}$	1.9 ± 0.5	2.0 ± 0.5	3.9 ± 0.1
$\tau(\mathrm{fm}/c)$	$3.44^{+1.1}_{-1.5}$	3.6 ± 0.8	4.7 ± 0.5	5.8 ± 0.4
λ	0.63 ± 0.04	0.75 ± 0.1	0.65 ± 0.05	0.88 ± 0.03
χ^2/NDF	$80.3/96$	$145/160$	$389/408$	$846/795$
$\chi^2_{\mathrm{PML}}/\mathrm{NDF}$	$211.2/158$	$1716/1663$	$2195/1927$	$2607/2098$
Events	6700	3300	8400	$39{,}100$

TABLE VIII. Parameters as a function of the projectile, for the 45° uncut data.

Projectile	45° Data, Uncut		
	Ar	Fe	Nb
$R_\perp$(fm)	4.5 ± 1.0	4.0 ± 0.65	4.8 ± 0.55
$R_\parallel$(fm)	1.0 ± 1.0	$1.5^{+0.55}_{-0.9}$	3.8 ± 0.2
τ(fm/c)	$0.0^{+2.3}_{-0.0}$	1.7 ± 1.7	4.8 ± 1.0
λ	0.72 ± 0.10	0.66 ± 0.06	0.89 ± 0.035
χ^2/NDF	138/156	381/403	846/795
χ^2_{PML}/NDF	1702/1662	2194/1925	2612/2098
Events	3300	8400	39,100

TABLE IX. Parameters as a function of the projectile, for the 45° data with $|\mathbf{p}_{\mathrm{cm}}| >$ 150 MeV/c. There is not enough data in the Ar sample to fit the data with the cut.

Projectile	45° Data, $|\mathbf{p}_{\mathrm{cm}}| > 150$ MeV/c	
	Fe	Nb
$R_\perp$(fm)	$4.3^{+0.6}_{-0.8}$	5.2 ± 0.55
$R_\parallel$(fm)	$1.5^{+0.6}_{-1.0}$	4.1 ± 0.2
τ(fm/c)	$0.1^{+2.8}_{-0.1}$	5.0 ± 1.1
λ	0.58 ± 0.07	0.87 ± 0.035
χ^2/NDF	362/345	742/719
χ^2_{PML}/NDF	2167/1897	2477/1945
Events	6900	34,600

TABLE X. Parameters as a function of the projectile, for the 0° data with $|\mathbf{p}_{\mathrm{proj}}| >$ 50 MeV/c.

	0° Data, $|\mathbf{p}_{\mathrm{proj}}| > 50$ MeV/c			
Projectile	Ar	Fe	Nb	Nb (π^+)
$R_\perp$(fm)	4.8 ± 0.3	4.8 ± 0.2	5.1 ± 0.2	5.3 ± 1.0
$R_\parallel$(fm)	4.2 ± 0.4	2.7 ± 0.3	4.4 ± 0.3	7.4 ± 1.2
τ(fm/c)	$1.1^{+1.4}_{-1.1}$	2.7 ± 0.6	3.9 ± 0.4	$0.0^{+3.6}_{-0.0}$
λ	0.81 ± 0.06	0.88 ± 0.03	1.11 ± 0.03	1.0 ± 0.17
χ^2/NDF	581/537	939/729	1144/1087	69/86
χ^2_{PML}/NDF	2979/2590	2938/2420	3776/3235	736/753
Events	12,900	3200	49,400	1700

TABLE XI. Parameters as a function of the projectile, for the 0° data with $|\mathbf{p}_{\mathrm{proj}}| >$ 100 MeV/c.

	0° Data, $|\mathbf{p}_{\mathrm{proj}}| > 100$ MeV/c		
Projectile	Ar	Fe	Nb
$R_\perp$(fm)	3.7 ± 0.4	4.7 ± 0.3	4.6 ± 0.3
$R_\parallel$(fm)	3.0 ± 0.5	2.1 ± 0.5	4.5 ± 0.3
τ(fm/c)	2.7 ± 0.8	3.5 ± 0.7	3.8 ± 0.5
λ	0.9 ± 0.10	0.75 ± 0.05	1.05 ± 0.04
χ^2/NDF	324/318	470/395	665/630
χ^2_{PML}/NDF	2147/1936	1476/1300	2386/2091
Events	6800	11,200	21,400

TABLE XII. Parameters for two different cuts on the average of the pion momentum, for the $0°$ Nb + Nb data with $|\mathbf{p}_{\mathrm{proj}}| > 50$ MeV/c.

$|\langle \mathbf{p} \rangle|$	Nb, $0°$ Data, $|\mathbf{p}_{\mathrm{proj}}| > 50$ MeV/c	
	0–225 MeV/c	225–500 MeV/c
$R_\perp(\mathrm{fm})$	5.0 ± 0.3	4.8 ± 0.3
$R_\parallel(\mathrm{fm})$	4.4 ± 0.3	4.8 ± 0.3
$\tau(\mathrm{fm}/c)$	3.5 ± 0.5	4.1 ± 0.7
λ	1.31 ± 0.03	1.19 ± 0.06
χ^2/NDF	536/503	1037/987
$\chi^2_{\mathrm{PML}}/\mathrm{NDF}$	1529/1485	2775/2587
Events	25,700	23,700

TABLE XIII. Parameters for two different cuts on the average of the pion momentum, for the $45°$ Nb + Nb uncut data.

$|\langle \mathbf{p} \rangle|$	Nb, $45°$ Data	
	0–225 MeV/c	225–650 MeV/c
$R_\perp(\mathrm{fm})$	$4.5^{+0.9}_{-0.5}$	$4.3^{+0.9}_{-1.1}$
$R_\parallel(\mathrm{fm})$	3.9 ± 0.3	4.1 ± 0.3
$\tau(\mathrm{fm}/c)$	6.0 ± 1.2	5.7 ± 1.5
λ	0.84 ± 0.04	$0.94^{+0.11}_{-0.07}$
χ^2/NDF	323/332	788/723
$\chi^2_{\mathrm{PML}}/\mathrm{NDF}$	736/716	2687/2012
Events	15,200	23,900

TABLE XIV. Pion-source parameters for different projectile-target combinations. The data marked with an asterisk were biased towards central collisions beyond the biasing occurs due to the spectrometer's acceptance.

Projectile	Target	E (GeV/nucleon)	R_{rms} (fm)	Reference
p	H	200	1.66 ± 0.04	41
p	Xe	200	1.53 ± 0.13	41
p	Xe	200	1.45 ± 0.11	41*
d	Ta	3.4	2.20 ± 0.50	42
He	Ta	3.4	2.90 ± 0.40	42
C	C	3.4	2.75 ± 0.73	43
C	C	3.4	3.76 ± 0.88	43*
C	Ta	3.4	3.40 ± 0.30	42
Ne	NaF	1.8	$2.24^{+0.98}_{-1.96}$	20
Ar	KCl	1.8	$3.39^{+0.73}_{-1.10}$	20
Ar	KCl	1.5	5.76 ± 0.61	36
Ar	KCl	1.2	4.65 ± 0.61	36*
Ar	BaI_2	1.8	3.75 ± 1.35	44
Ar	Pb_3O_4	1.8	4.04 ± 1.14	44
Ar	Pb_3O_4	1.8	4.87 ± 0.96	44*
Ar	KCl	1.8	2.3 ± 0.6	this work
Fe	Fe	1.7	2.5 ± 0.6	this work
Kr	RbBr	1.2	6.61 ± 1.47	45
Nb	Nb	1.5	4.8 ± 0.1	this work

TABLE XV.   Comparison between experimental and CASCADE pion-source parameters for the 45° data. The data marked (Zajc) are the Ar π^- data of Zajc *et al.*;[20] the remaining experimental data are this work. Only statistical uncertainties are shown.

| | Ar, 45° Data, Single-Radius-Parameter Fit | | |
	Experiment (Zajc)	This Experiment	CASCADE
R(fm)	$2.77^{+0.6}_{-0.9}$	1.9 ± 0.5	3.58 ± 0.11
τ(fm/c)	$3.44^{+1.1}_{-1.5}$	3.6 ± 0.8	2.83 ± 0.43
λ	0.63 ± 0.04	0.75 ± 0.1	1.003 ± 0.045
χ^2/NDF	80.3/96	145/160	–
$\chi^2_{\rm PML}$/NDF	211.2/158	1716/1663	–
Events	6700	3300	–

TABLE XVI. Comparison between experimental and CASCADE pion-source parameters for the Fe data. The uncertainties shown for the measured data are total. The uncertainties shown for CASCADE are statistical only.

	Fe, 45° Data		Fe, 45° Data	
	$|\mathbf{p}_{cm}| > 100$ MeV/c (uncut)		$|\mathbf{p}_{cm}| > 150$ MeV/c	
	Experiment	CASCADE	Experiment	CASCADE
$R_\perp$(fm)	4.0 ± 0.65	4.2 ± 0.3	$4.3^{+0.6}_{-0.8}$	4.2 ± 0.2
$R_\parallel$(fm)	$1.5^{+0.55}_{-0.9}$	3.0 ± 0.2	$1.5^{+0.6}_{-1.0}$	2.9 ± 0.2
τ(fm/c)	1.7 ± 1.7	3.3 ± 0.6	$0.1^{+2.8}_{-0.1}$	3.2 ± 0.6
λ	0.66 ± 0.06	1.00 ± 0.02	0.58 ± 0.07	0.98 ± 0.02
χ^2/ NDF	381/403	1099/1082	362/345	1112/1039
χ^2_{PML}/NDF	2194/1925	1563/1691	2167/1897	1596/1708

|	Fe, 0° Data		Fe, 0° Data	
	$|\mathbf{p}_{proj}| > 50$ MeV/c		$|\mathbf{p}_{proj}| > 100$ MeV/c	
	Experiment	CASCADE	Experiment	CASCADE
$R_\perp$(fm)	4.8 ± 0.2	4.0 ± 0.1	4.7 ± 0.3	4.4 ± 0.1
$R_\parallel$(fm)	2.7 ± 0.3	3.3 ± 0.1	2.1 ± 0.5	2.3 ± 0.1
τ(fm/c)	2.7 ± 0.6	4.3 ± 0.2	3.5 ± 0.7	4.4 ± 0.2
λ	0.88 ± 0.03	1.00 ± 0.02	0.75 ± 0.05	0.98 ± 0.02
χ^2/ NDF	939/729	1031/1061	470/395	374/376
χ^2_{PML}/NDF	2938/2420	1543/1693	1476/1300	498/555
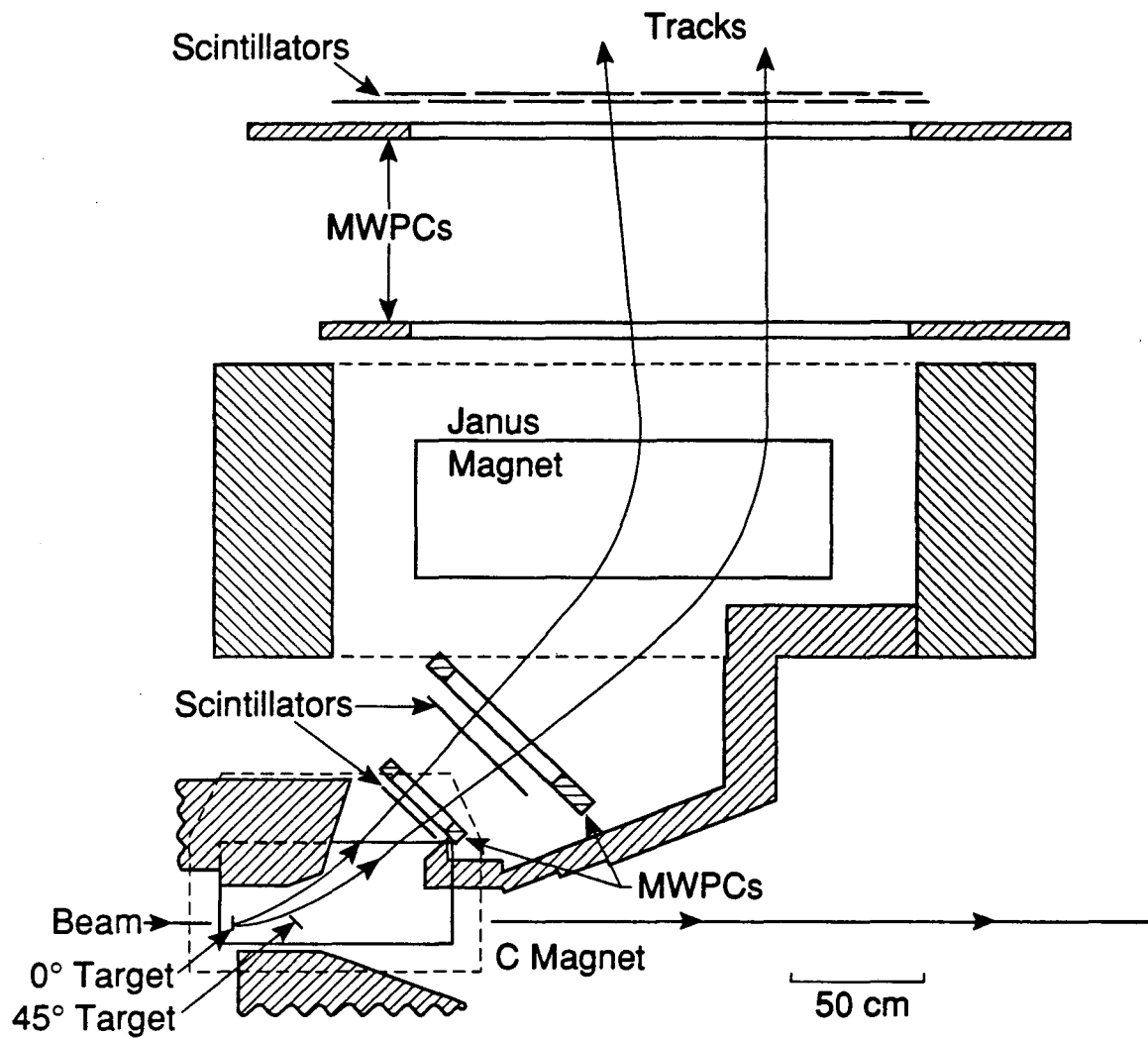
FIG. 1. Plan View of the Janus spectrometer as used in the Ar and Nb runs. In the earlier Fe run part of the lead wall between the second wire chamber (MWPC) and beam line was absent and a different second wire chamber (where the wire chamber numbering follows the the path of the particles, starting at the target) was used.

45° Data

0° Data

B

A

B

A
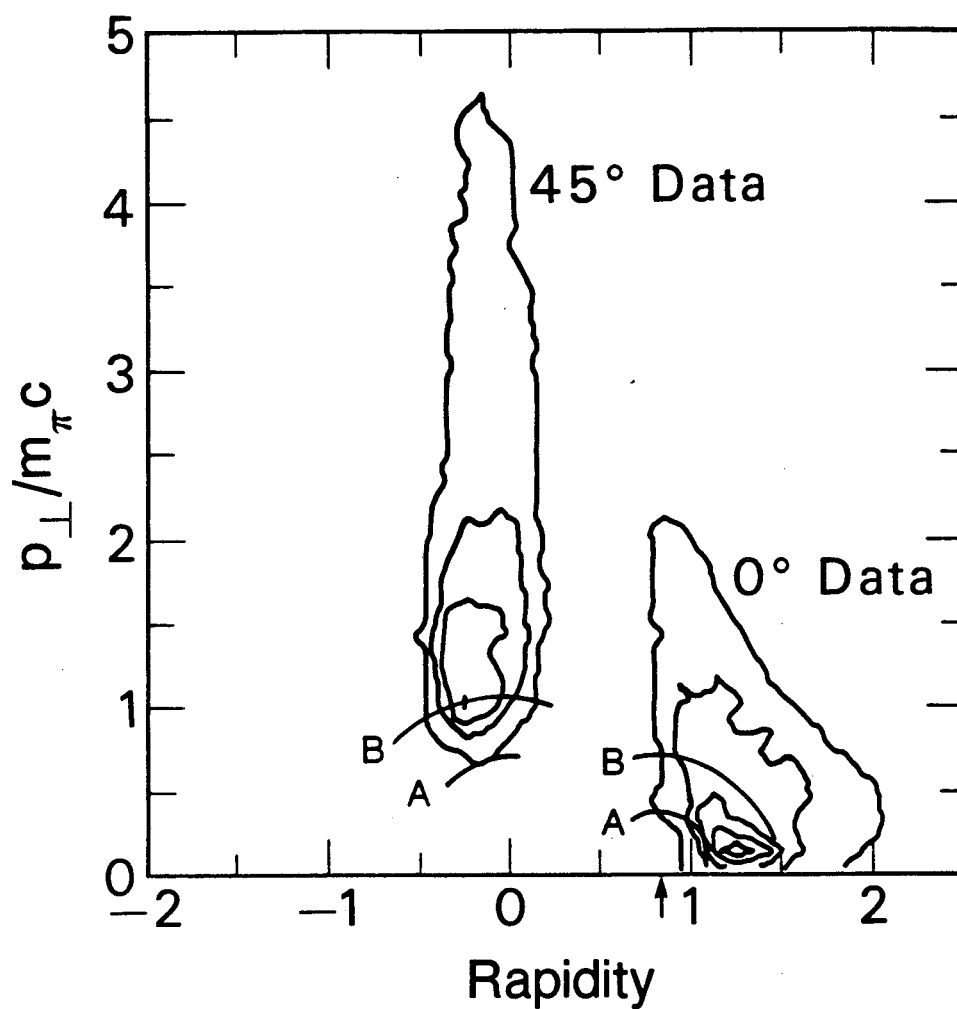
XBL 867-8852 A

FIG. 2.   Contour plot of the acceptance for the 45° and the 0° Fe configurations. The arrow marks the beam rapidity. The lines marked "A" indicate the lower momentum cut employed for each acceptance, the lines marked "B" indicate the higher of the momentum cuts.
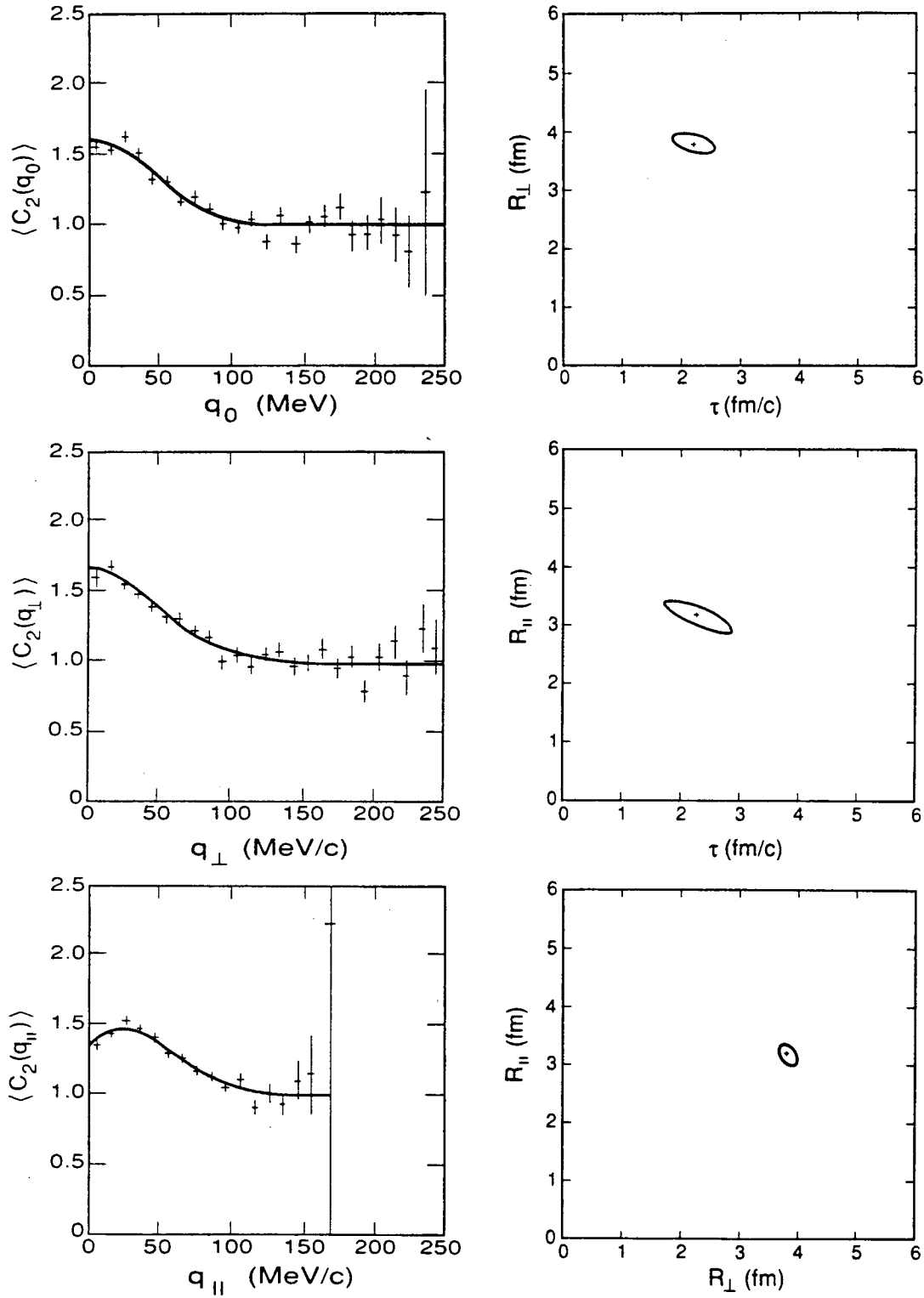
FIG. 3. Correlation function projections and one standard deviation confidence contours for fits using the Monte Carlo data. Left column: the projections for $\langle C(q_0)\rangle$, $\langle C(q_\perp)\rangle$ and $\langle C(q_{\|})\rangle$. Only statistical uncertainties are shown. Right Column: the confidence contours for the $R_\perp$ vs. τ plane, the $R_{\|}$ vs. τ plane and the $R_{\|}$ vs. $R_\perp$ plane.
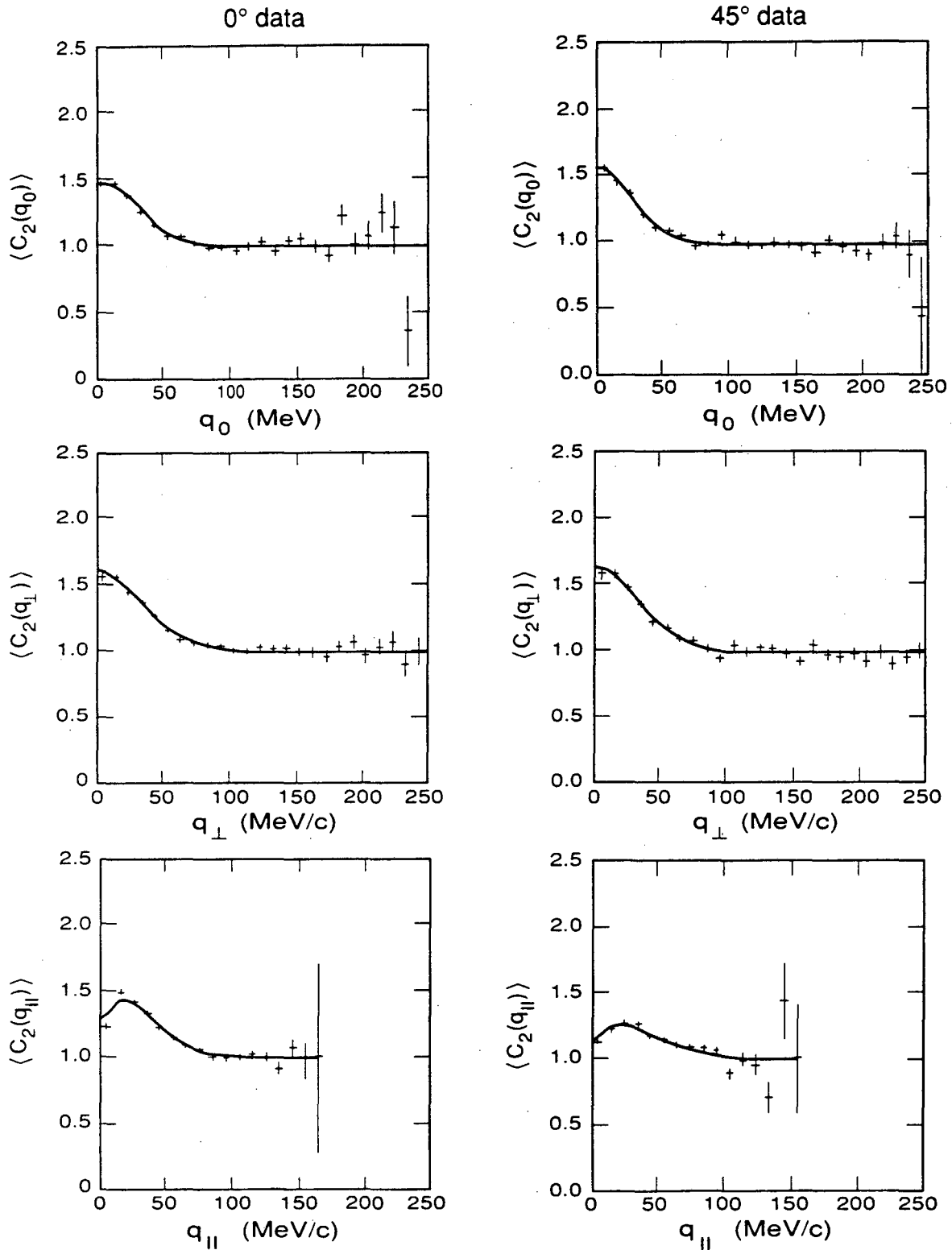
FIG. 4. Correlation function projections for the least-cut Nb data samples. Left column: the projections for the 0° Nb data with $|p_{proj}| > 50$ MeV/c. Right column: the projections for the 45° Nb data with $|p_{cm}| > 110$ MeV/c. Only statistical uncertainties are shown.
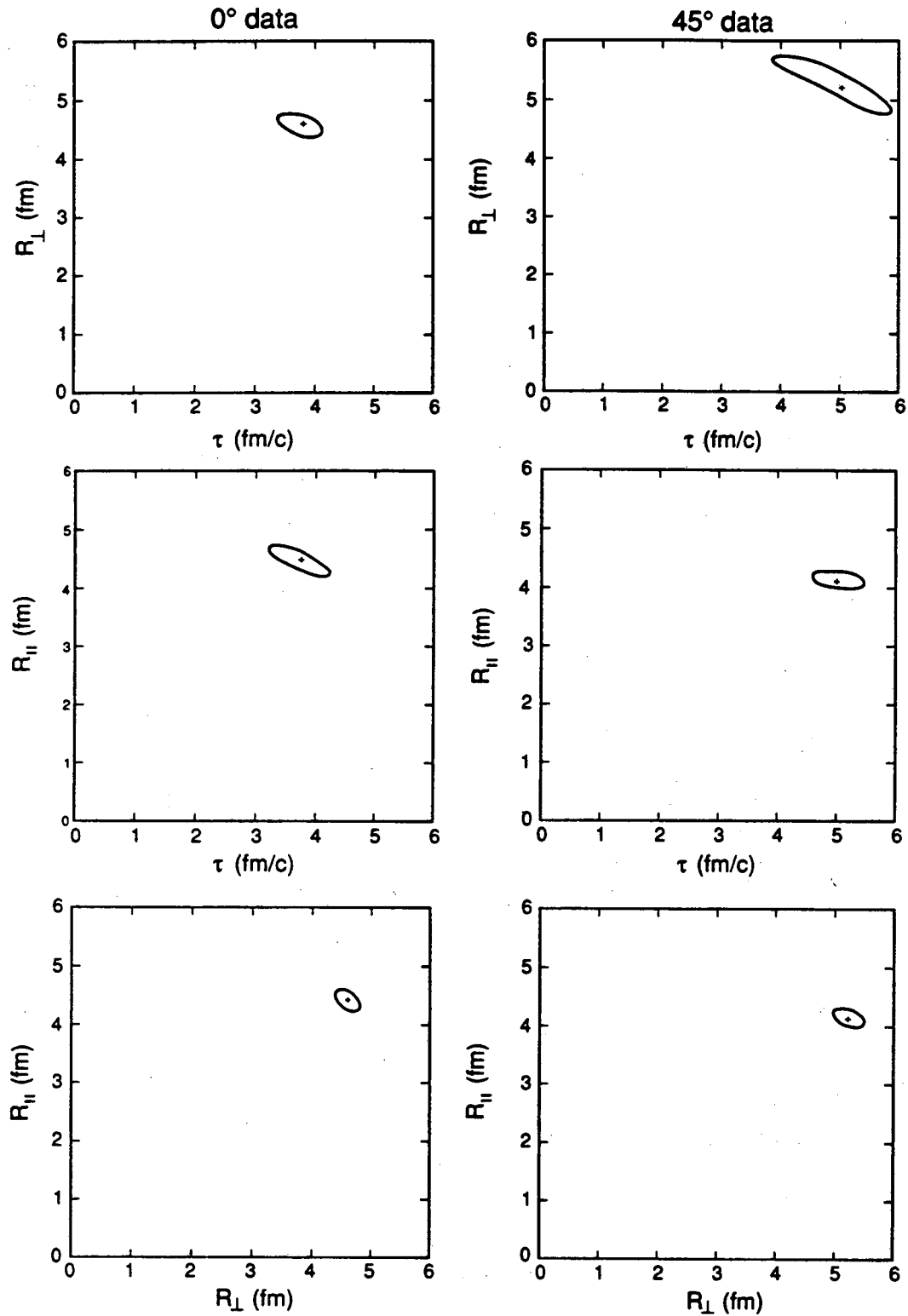
FIG. 5. The one standard deviation confidence contours for the most-cut Nb data. Left column: the $0°$ Nb data with $|\mathbf{p}_{proj}| > 100$ MeV/c. Right column: the $45°$ Nb data with $|\mathbf{p}_{cm}| > 150$ MeV/c.

55
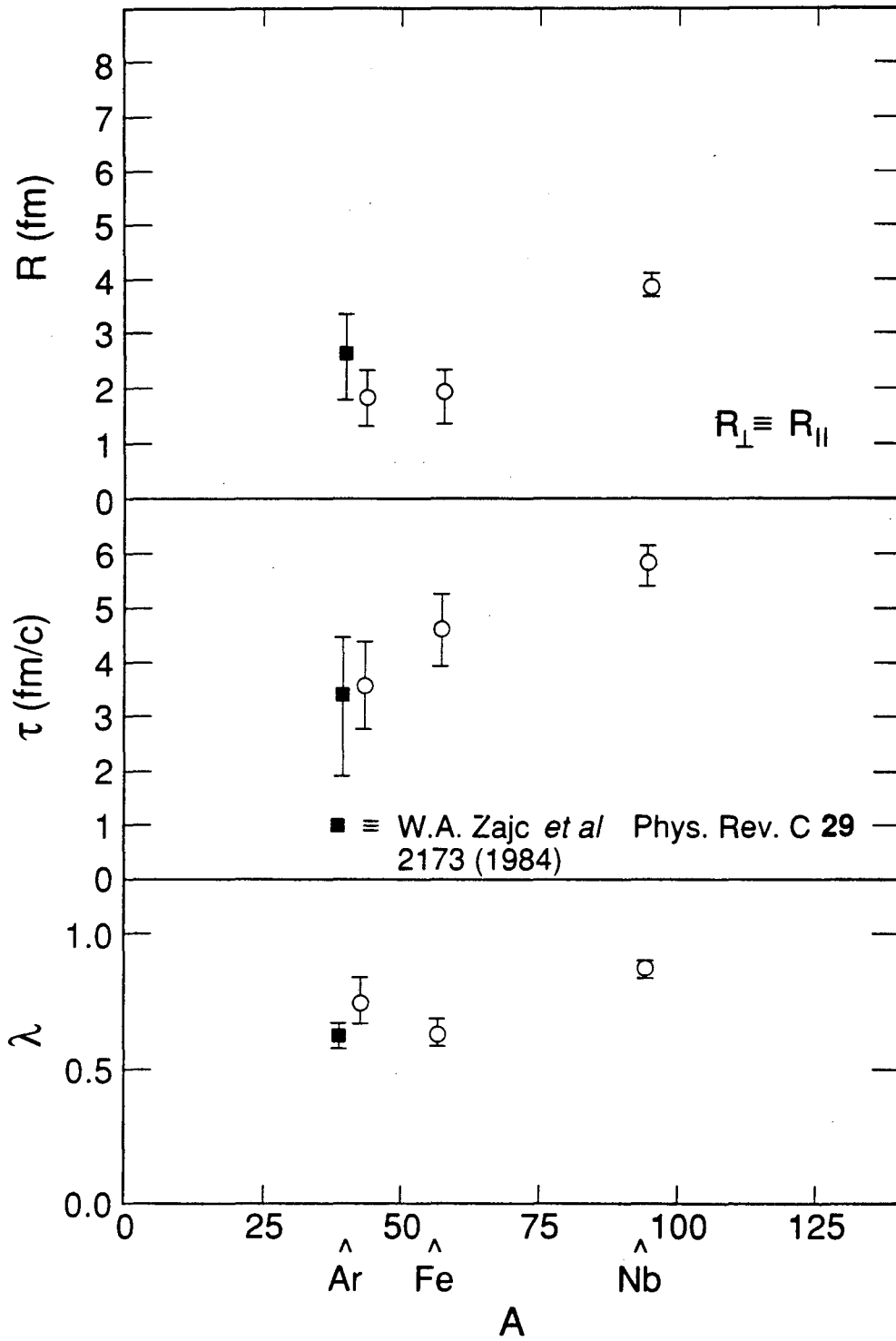
FIG. 6. Fit parameters as a function of A for the 45° data with $R_\perp \equiv R_{||}$. The data points for Ar have been displaced for clarity. Only statistical uncertainties are shown.
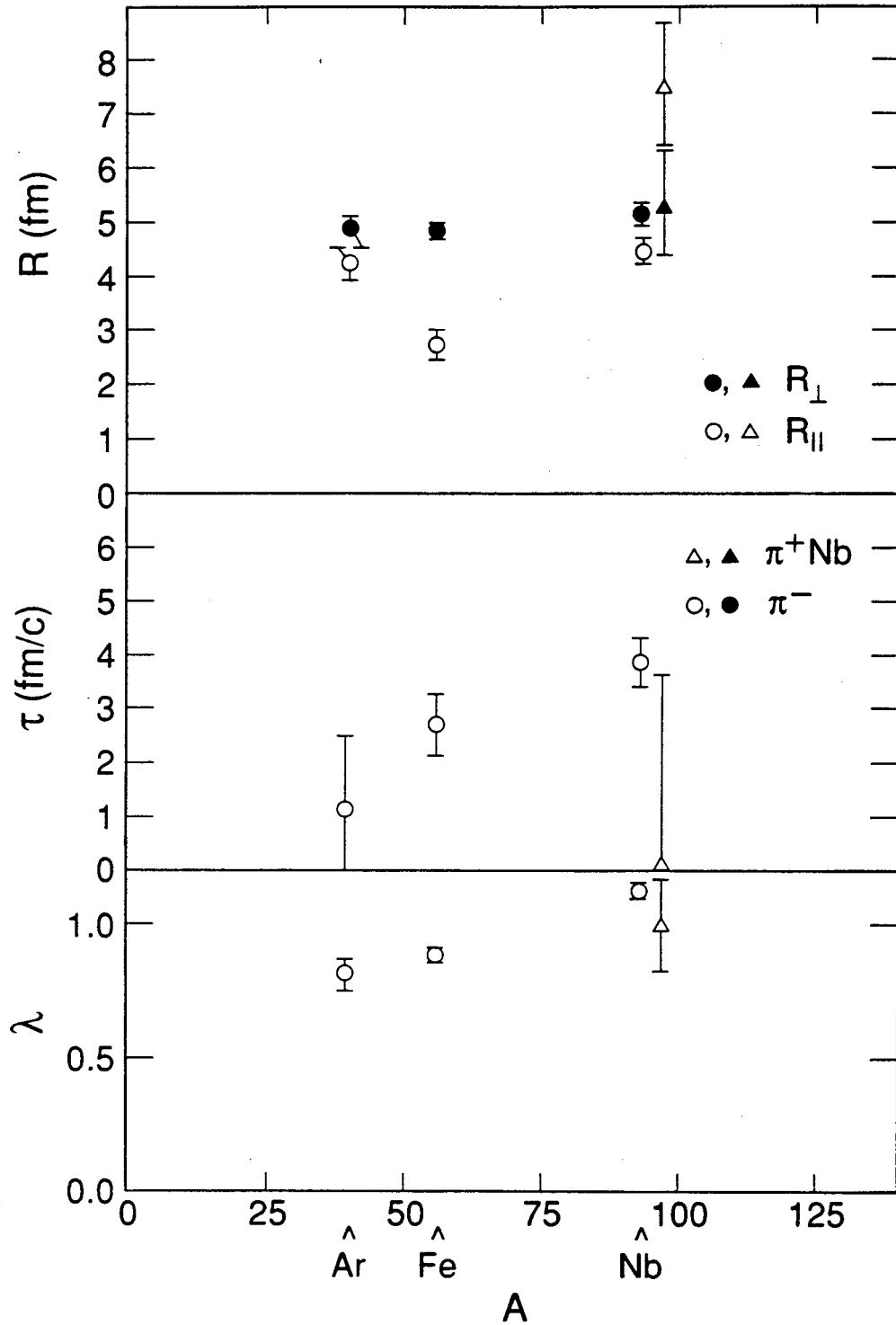
XBL 899-7740A

56
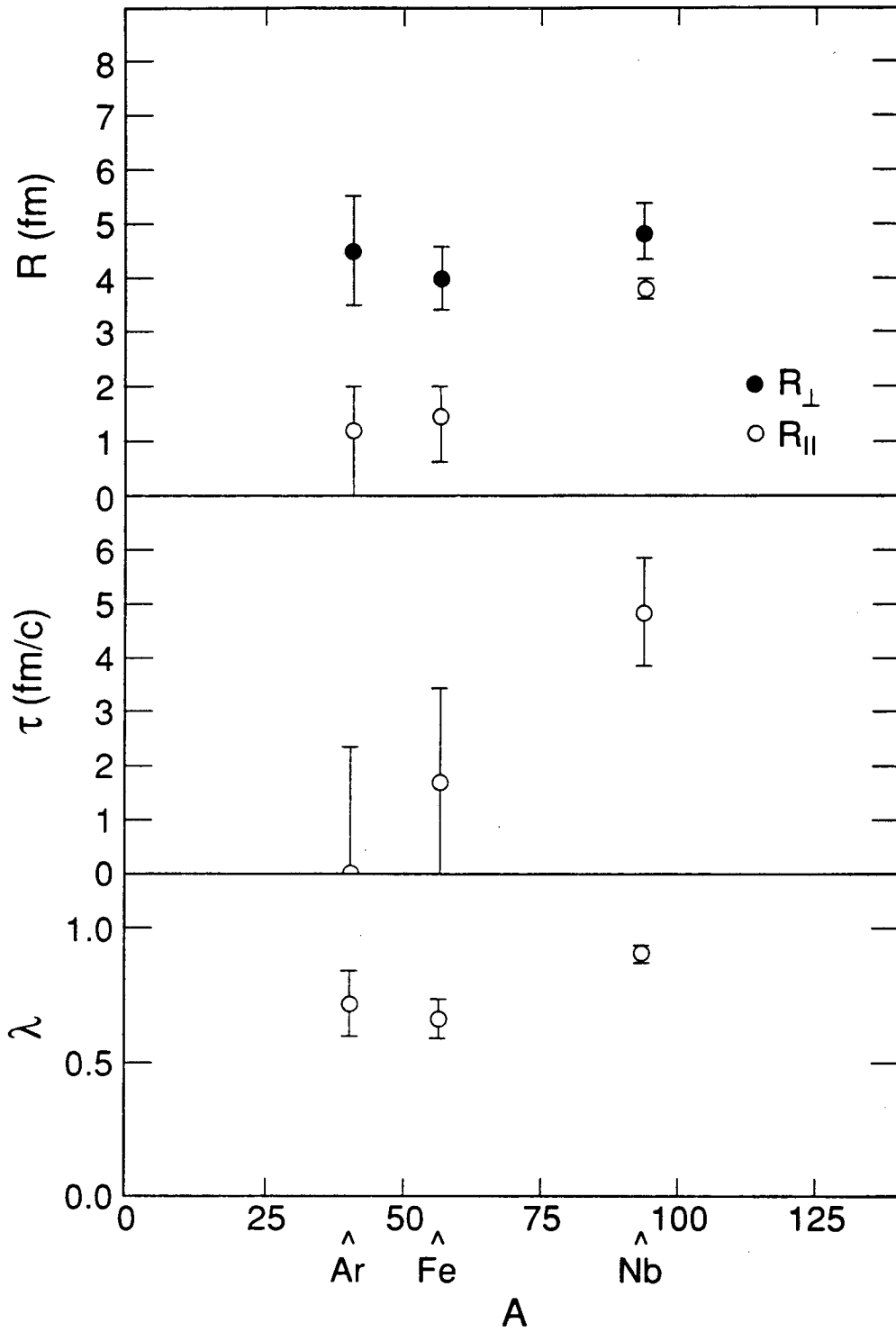
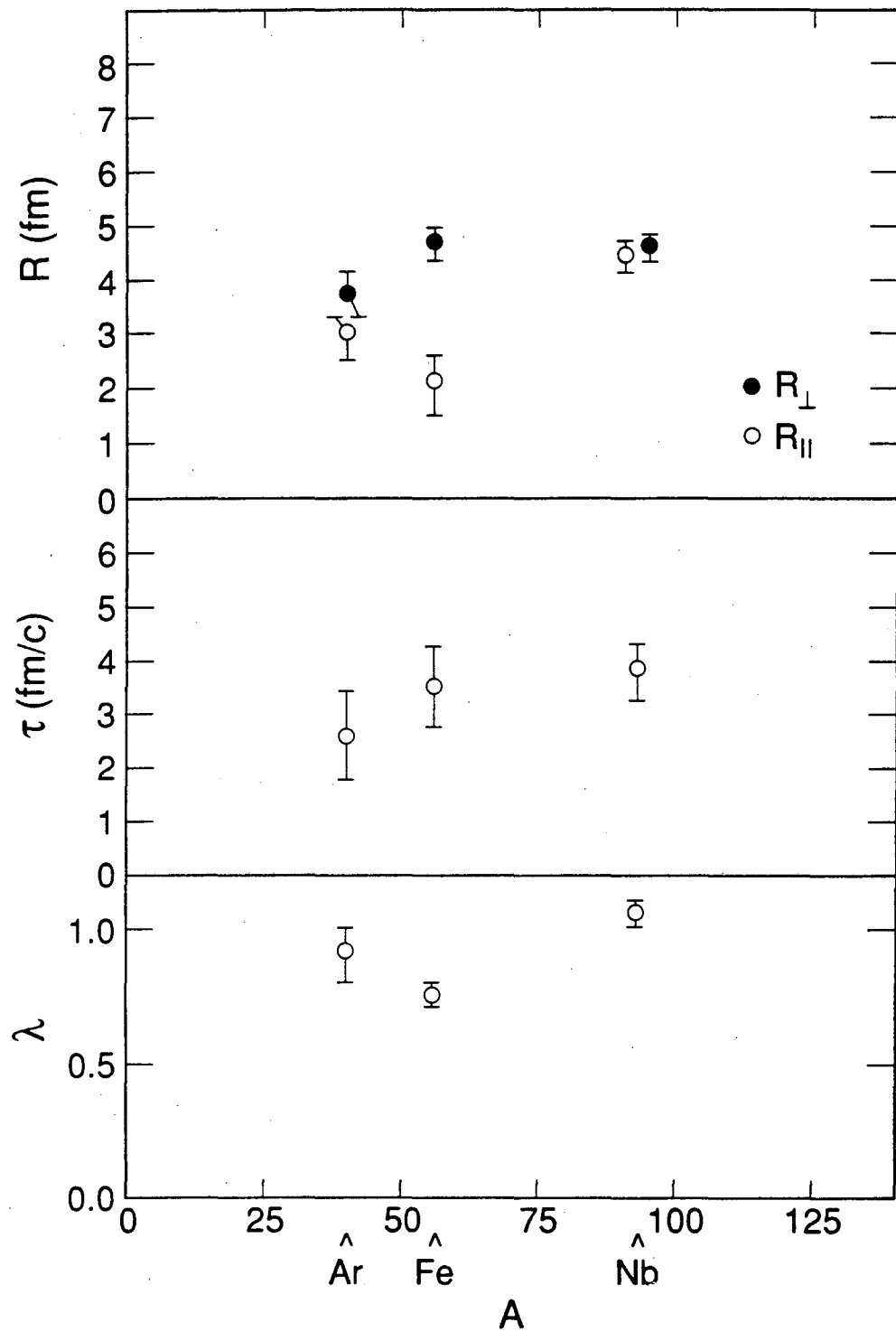FIG. 7. Fit parameters as a function of A for the 45° uncut data.
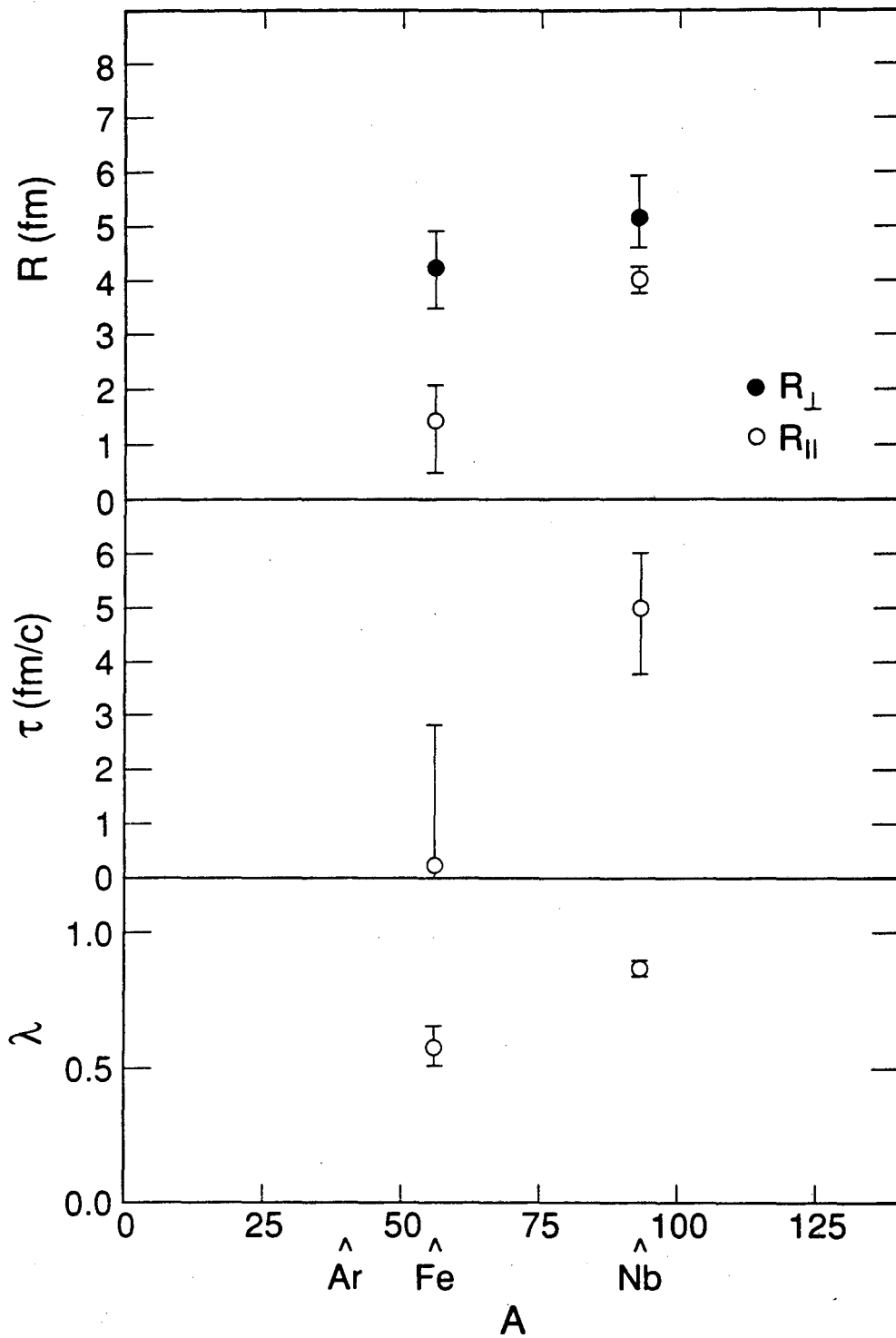
XBL 899-7739A

FIG. 8. Fit parameters as a function of A for the 45° data with a momentum cut imposed.

58

FIG. 9. Fit parameters as a function of A for the $0°$ least-cut data. The data points for Nb have been displaced for clarity. The circles (triangles) denote parameters extracted from π^- (π^+) data. For the radius parameters, the open symbols denote $R_{\parallel}$ and the closed symbols denote $R_{\perp}$.

59

FIG. 10. Fit parameters as a function of A for the 0° data with a momentum cut imposed. The data points for the Nb radii have been displaced for clarity.

XBL 899-7738A

60
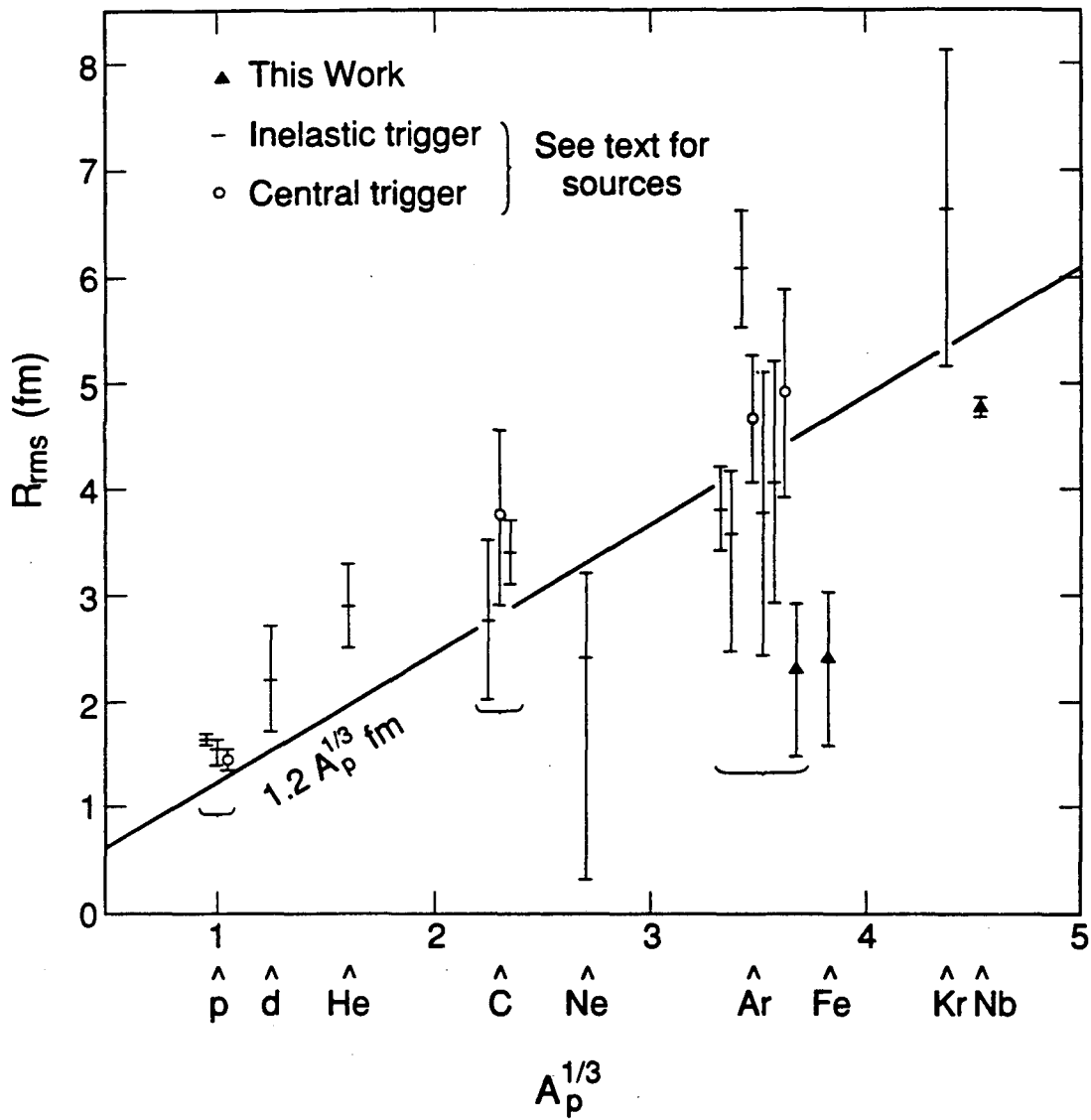
FIG. 11. Pion-source parameters as a function of $A_p^{1/3}$, where A_p is the atomic mass of the projectile. The data are from the sources listed in Table XIV. The data points for some projectiles have been displaced for clarity.

XBL 899-7727A

61

LAWRENCE BERKELEY LABORATORY
UNIVERSITY OF CALIFORNIA
INFORMATION RESOURCES DEPARTMENT
BERKELEY, CALIFORNIA 94720